remote sensing

Article

Evaluation of Atmospheric Correction Algorithms over Lakes for High-Resolution Multispectral Imagery: Implications of Adjacency Effect

Yanqun Pan [1,*,†], Simon Bélanger [1] and Yannick Huot [2]

1 Département de biologie, Chimie et Géographie, Groupes BORÉAS et Québec Océan, Université du Québec à Rimouski, Rimouski, QC G5L 3A1, Canada; simon_belanger@uqar.ca
2 Département de Géomatique Appliquée, Université de Sherbrooke, Sherbrooke, QC J1K 2R1, Canada; yannick.huot@usherbrooke.ca
* Correspondence: yp@arctus.ca
† Present address: Arctus Inc., Rimouski, QC G5L 3A1, Canada.

Abstract: Atmospheric correction of satellite optical imagery over inland waters is a key remaining challenge in aquatic remote sensing. This is due to numerous confounding factors such as the complexity of water optical properties, the surface glint, the heterogeneous nature of atmospheric aerosols, and the proximity of bright land surfaces. This combination of factors makes it difficult to retrieve accurate information about the system observed. Moreover, the impact of radiance coming from adjacent land (adjacency effects) in complex geometries further adds to this challenge, especially for small lakes. In this study, ten atmospheric correction algorithms were evaluated for high-resolution multispectral imagery of Landsat-8 Operational Land Imager and Sentinel-2 MultiSpectral Instrument using in situ optical measurements from ~300 lakes across Canada. The results of the validation show that the performance of the algorithms varies by spectral band and evaluation metrics. The dark spectrum fitting algorithm had the best performance in terms of similarity angle (spectral shape), while the neural network-based models showed the lowest errors and bias per band. However, none of the tested atmospheric correction algorithms meet a 30% retrieval accuracy target across all the visible bands, likely due to uncorrected adjacency effects. To quantify this process, three-dimensional radiative transfer simulations were performed and compared to satellite observations. These simulations show that up to 60% of the top of atmosphere reflectance in the near-infrared bands over the lake was from the adjacent lands covered with green vegetation. The significance of these adjacency effects on atmospheric correction has been analyzed qualitatively, and potential efforts to improve the atmospheric correction algorithms are discussed.

Keywords: atmospheric correction; Sentinel-2; Landsat-8; adjacency effect; 3D radiative transfer

check for updates

Citation: Pan, Y.; Bélanger, S.; Huot, Y. Evaluation of Atmospheric Correction Algorithms over Lakes for High-Resolution Multispectral Imagery: Implications of Adjacency Effect. *Remote Sens.* **2022**, *14*, 2979. https://doi.org/10.3390/rs14132979

Academic Editors: Cédric Jamet and Jae-Hyun Ahn

Received: 12 May 2022
Accepted: 20 June 2022
Published: 22 June 2022

1. Introduction

Lakes are important ecosystems providing various ecosystem services including the provision of drinking water for humans and animals [1]. They play a crucial role in the terrestrial hydrological cycle through complex processes at their interfaces with the atmosphere and oceans and are valuable natural resources [2]. However, stressors such as eutrophication or climate change threaten their ecological functions [3,4]. The Global Climate Observing System (GCOS) of the World Meteorological Organization has recognized "Lakes" as one of its Essential Climate Variables. In the past decades, several national and international directives have addressed these problems and aimed to improve the ecological state of inland waters by identifying stressors and by implementing sustainable management strategies supported by sporadic monitoring [5–8]. In 2016, to provide Canada's first national assessment of lake health, the Natural Sciences and Engineering Research Council of Canada (NSERC) Canadian Lake Pulse Network was launched [9] (hereafter referred to as 'LakePulse'). LakePulse uses traditional in situ approaches for limnological monitoring as well as state-of-the-art methods, such as optical remote sensing.

Remote sensing has long been promised as a tool for large-scale monitoring of inland water quality [10]. Dating back to the early 1970s, airborne and satellite sensors have been used to examine a wide range of water quality constituents [2,11]. Due to the limitation of spatial resolution, ocean color satellites sensors, e.g., Coastal Zone Color Scanner (CZCS), Sea-viewing Wide Field-of-view Sensor (SeaWiFS), Medium Resolution Imaging Spectrometer (MERIS), and Moderate Resolution Imaging Spectroradiometer (MODIS) were rarely applied to inland waters with exception of large lakes such as the North American Great Lakes [12,13]. As an alternative, satellites dedicated to terrestrial surveillance with a relatively high spatial resolution, such as Landsat Multispectral Scanner (MSS), Thematic Mapper ™, Enhanced Thematic Mapper (ETM), and Advanced Land Imager (ALI), were used to quantify the water quality properties of lakes, including lake clarity, chlorophyll-a concentration (Chla), suspended particulate matter (SPM), colored dissolved organic matter (CDOM), etc. [14–27]. However, accurate water quality parameter retrieval requires a sensor with sufficient signal-to-noise ratio (SNR) over waters to measure and separate the small water-leaving signal from other sources of radiance reaching the sensor, and the low SNR of historical Landsat sensors led to poor quality imagery for use on lakes. This situation changed with the launch of a new generation of satellites (Landsat-8, Sentinel-2) offering unprecedented capabilities [28]. The existing sensors, Operational Land Imager (OLI) and Multispectral Imager (MSI) have much better SNR and spatial resolution, 30 and 10 m, respectively, providing great potential applications in lakes including smaller lakes with sizes in the hundreds of meters.

Atmospheric correction (AC) is a procedure to remove the signal at the sensor (i.e., top of atmosphere, TOA), the radiance contributions from the atmosphere and the water surface, in order to derive the radiance leaving the water body (the so-called water-leaving radiance) [29], which is one of the key processing steps for allowing the remote sensing of water color [30]. During atmospheric correction over water, remote sensing reflectance ($R_{rs}(\lambda)$, sr^{-1}), is defined as the ratio of water-leaving radiance ($L_w(\lambda)$, $\mu W/[cm^2\ nm\ sr]$) to downwelling irradiance above the water surface ($E_d(0^+, \lambda)$, $\mu W/[cm^2\ nm]$) (see review by Mobley [31]), is obtained from TOA measurements. AC in aquatic remote sensing has been studied for several decades, and numerous algorithms have been proposed for ocean color satellite imagery over coastal and inland waters. Recently, some of these algorithms were tuned for the new generation of satellites dedicated to land monitoring (Landsat-8 and Sentinel-2), while others have been specifically developed for these satellites. Despite the paramount importance of accurate AC for robust retrievals of optical water constituents [32], it remains one of the largest sources of error for inland and coastal waters [33,34]. Understanding the performance limitations and key sources of errors in these algorithms for regional and global waters is critical to the remote sensing community and to managers who depend on the downstream data. In recent years, a few studies have been conducted on a regional and global scale to do so. For example, Warren et al. [35] and Pereira-Sandoval et al. [36] assessed most AC algorithms developed for MSI over European coastal and inland waters. Basically, their results showed all ACs tests showed large uncertainties, and their performance varied as a function of water types. In general, C2RCC [37,38] and Polymer [39] provided the best statistics, but ACOLITE [40], iCOR [41] and Sen2Cor [42] had better performance when applied to meso- and hyper-eutrophic waters, compared with oligotrophic waters. More recently, an international effort supported by space agencies (NASA and ESA), i.e., the atmospheric correction inter-comparison exercise for global coastal and inland waters (ACIX-Aqua) investigated the performance of ACs [34]. This matchup exercise aimed at performing a comprehensive evaluation of water reflectance products produced via eight AC processors using a large in situ optical dataset (>2000 samples) collected under various atmospheric conditions and in different coastal and inland environments across the globe. However, in situ data collected in small lakes, including those from the Canadian dataset collected as part of LakePulse (110 samples), were excluded from the exercise due to large sources of errors in the retrieved $R_{rs}(\lambda)$ likely stemming from adjacency effects that led to unacceptable errors (>100%).

Generally, the reduction of image contrast when the atmospheric scattering increases, the so-called adjacency effect (hereafter AE) [43,44], makes the darker target appear brighter, and the brighter target becomes darker when a non-uniform surface is observed at TOA. In other words, AE leads to additional sources of radiance at the TOA measurement over a relatively darker target [45–47]. The AE is particularly strong over low reflectance targets in regions where sharp contrasts of reflectance exist such as water-land transition [48,49]. This water-land transition could include water pixels up to 30 km from shore [50,51]. Since the surface reflectance of waters and the surrounding lands and thus the contrast could change seasonally, the extent of AE also features seasonal changes [52]. In addition to the contrast between adjacent surfaces, the atmosphere scattering (Rayleigh and aerosol) also determines AE [44,50,53–55]. Regarding the modeling of AE, 3D radiative transfer MonteCarlo simulations were extensively performed to simulate AE in coastal regions fully accounting for realistic atmospheric conditions, typical illumination, and observation conditions, reflectance by a roughened water surface, and the coastal morphology [50,56]. For coastal waters in the 3D simulation, the boundary of land and water can be simplified to be a line for easy simulation and analysis [50]. However, for lakes, the situation is more complicated when the size and irregular shape that influence the contrast between the target and the surrounding background must be taken into account. In this paper, we further examine the AE for typical lakes using satellite observations and 3D radiative transfer simulations.

To answer the questions of which AC algorithm is the best suited for Canadian lakes and whether it satisfies the water quality monitoring requirements, this study performed a similar exercise to ACIX-Aqua [34] but focused on ~300 small Canadian lakes. In addition, although the problem of AE over inland waters has been identified in several papers before [35,36,57,58], its impact on small lakes has never been quantified in the context of atmospheric correction. The impacts of AE on the atmospheric correction over small lakes and potential correction methods are also discussed in this paper.

2. Material and Methods

2.1. Study Area

Canada is a vast country (9,984,670 km^2) that stretches from the Atlantic Ocean in the East to the Pacific Ocean in the West and is bordered to the North by the Arctic Ocean. It includes many geo-climatic regions and vastly different geomorphology. According to the Ecological Land Classification (ELC) of Canada [59], the country is divided into 16 separate terrestrial ecozones (Figure 1). Boreal forests form a large part of temperate latitude, with taiga and tundra to the North and a mixture of prairies and deciduous and mixed forest in the South [60]. Arctic regions and the Rocky Mountains are often covered by ice and snow. The apparent optical properties (AOPs): the downwelling irradiance (E_d, μW/(cm^2 nm)), upwelling radiance (L_u, μW/(cm^2 nm sr)), the in-water vertical profile of upwelling irradiance (E_u, μW/(cm^2 nm)), etc., were measured in the summers of 2017, 2018, and 2019 in 333 lakes (Figure 1). Most lakes are located in forested zones, such that the land surrounding the lakes have high Near-Infrared (NIR) band reflectance. Because most Canadian lakes are clear (low turbidity) and small, the contrast between the lakes and the backgrounds leads to strong AE in the satellite imagery.

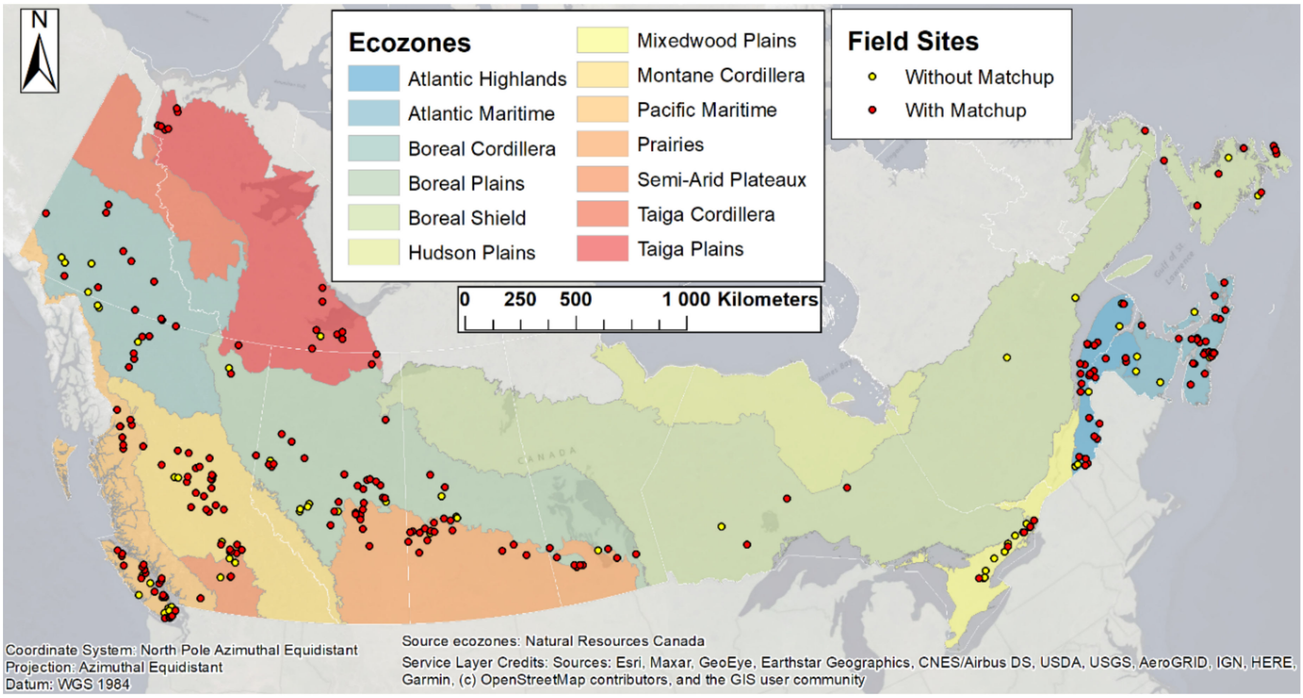

Figure 1. The ecozones of Canada and sampling stations (dots) with spectra that passed the quality control procedure from the LakePulse fieldwork of 2017, 2018, and 2019. Red dots are lakes with a matchup with either L8 or S2 satellite images.

2.2. In Situ Observation Data

The in situ data were collected as part of the LakePulse fieldwork campaign that occurred in the summers (from June to September) of 2017, 2018, and 2019. To quantitatively reflect the potential impact of altering land use on lake ecosystems, a human impact index was derived (see Huot et al. [9] for a description of the index). The value goes from 0 for no impact to 1 indicating lakes with a high likelihood of human impact. Most of the in situ measurements (Figure 2) were conducted in small (area < 5 km^2), shallow (depth < 10 m), low human-impacted (HII < 0.1) lakes, and low altitude regions (altitude < 500 m). The extremes for each category are 100 km^2 for the largest area, 130 m for the deepest, 0.9 for the highest human impact, and 1600 m for the lake at the highest altitude. Note that although most lakes are shallow (depth < 10 m), the waters are most likely to be optically deep due to high CDOM absorption. Average and ranges of variability for LakePulse data for SPM, Chla and CDOM absorption at 440 nm are 12.7 ± 135.4 mg/L, 9.7 ± 27.4 µg/L, and 3.66 ± 3.9 m^{-1}, respectively.

The radiometric data have been acquired with four different instruments: an in-water light profiler Compact-Optical Profiling System [61] (C-OPS; Biospherical Instruments Inc., San Diego, CA, USA), in-water TriOS-RAMSES hyperspectral radiometers (https://www.trios.de/, accessed on 16 June 2020), above-water Analytical Spectral Devices (ASD Inc., Boulder, CO, USA), and in-water Hyperspectral Ocean Color Radiometer (HyperOCR, https://www.seabird.com/hyperspectral-radiometers, accessed on 16 June 2020; SeaBird Scientific Inc., CO, USA). To reduce the influence of the bottom and shore, most of the measurements were taken in the deepest part of the lakes. Finally, the protocols recommended by the International Ocean-Colour Coordinating Group (IOCCG) for in situ optical radiometry were followed [62].

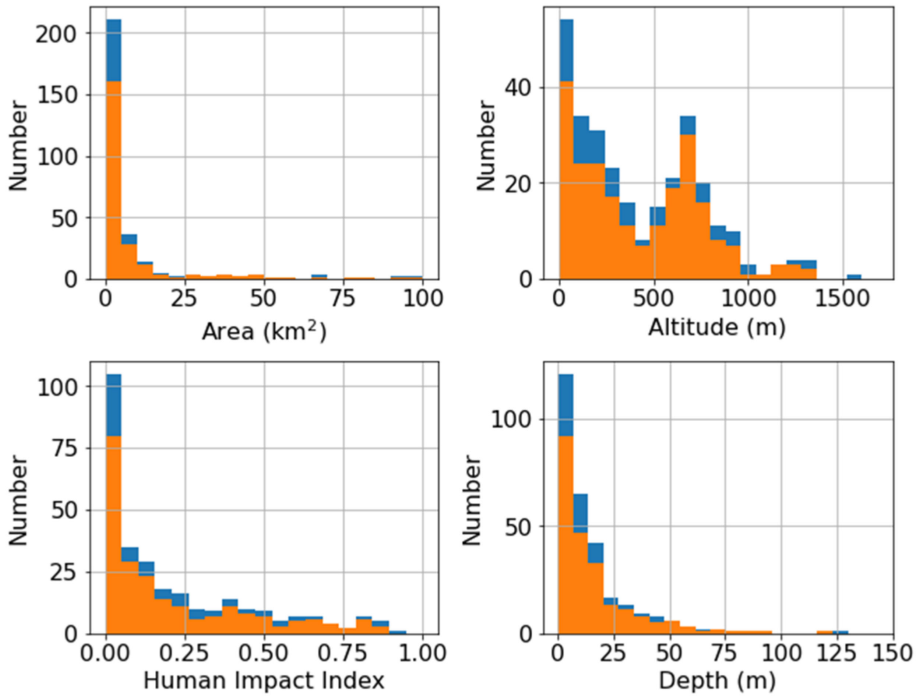

Figure 2. Distribution of the basic features (area, altitude, Human Impact Index and depth) of the sampled lakes that have the optical measurements (blue) and matchups (orange).

After processing and quality control (QC), 293 out of 333 R_{rs} spectra were kept from the fieldwork campaign for further analyses. The final R_{rs} dataset of 293 spectra contains 157 C-OPS, 62 ASD, 21 HOCR, and 53 TriOS-RAMSES measurements. The 293 R_{rs} spectra are classified into 13 inland water types as defined by Spyrakos et al. [63] based on the maximum correlation coefficient (r) of the standardized measured spectrum and the candidate water types, which are derived from the original spectrum divided by the area between each spectrum and a zero baseline, calculated in numerical integration. After applying this classification scheme, 10 out of 13 of the inland water types were found in the 293 spectra. For the spectra with a maximum $r < 0.80$, the water type was determined to be the 'other' type. Figure 3 shows the mean and standard deviation of the original (3a,b) and standardized (3c,d) R_{rs} spectra in each water type. The water type index and the number of spectra belonging to each water type connected with the symbol '-' are shown as the label of the legend. As shown, most spectra fall into "type 6" and "type 13", which represent a potential significant presence of cyanobacteria and clear blue water, respectively. In addition, most spectra show steep curves between 440–560, suggesting that the waters are potentially rich in CDOM.

The detailed methods of in situ data processing and quality control are described in Section 2.4. Note that TriOS-RAMSES, ASD, and HOCR record radiance using hyperspectral sensors with a resolution of ~3 nm, while the C-OPS has 19 bands with a bandwidth of 10 nm. In the field campaign, four different C-OPS owned by Université de Québec à Rimouski (UQAR), Laboratoire d'Océanographie de Villefranche (LOV), Laval university (Takuvik), and Université de Sherbrooke (UdeS), having slightly different band settings were used (see Supplementary Material). All C-OPS were calibrated by the manufacturer prior to each field campaign. The R_{rs} spectra measured by C-OPS shown in Figure 3 were linearly interpolated to 1 nm resolution, which were then converted to L8/OLI and S2/MSI sensor equivalent spectral bands based on the relative spectral response functions.

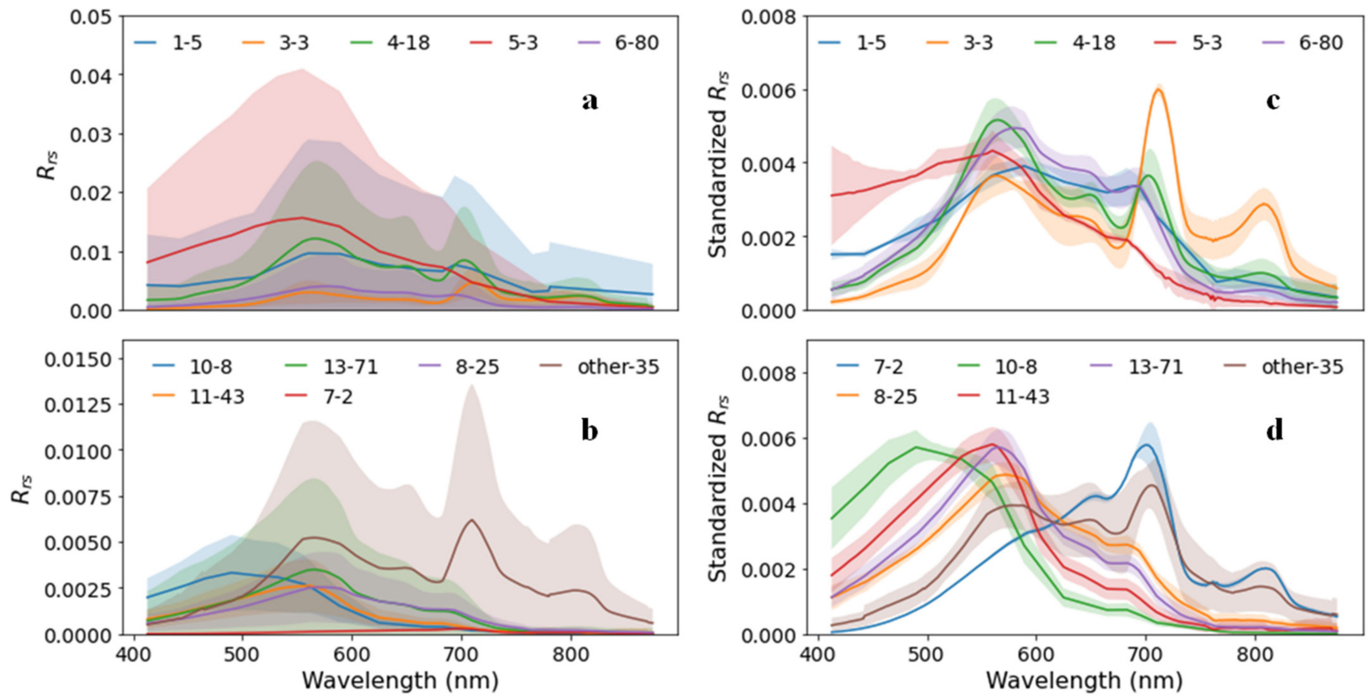

Figure 3. Rrs spectra used in this paper, collected in LakePulse fieldwork and their classifications. (**a**,**b**) Mean and standard deviation of the Rrs spectra for each inland water type (**c**,**d**) Mean and standard deviation of the standardized Rrs spectra for each inland water type. The labels of the legend represent the water type index [63] and the number of spectra belonging to each type connected by '-'.

2.3. Earth Observation Data

We obtained radiometrically calibrated data at the TOA from Landsat and Sentinel-2 satellite missions. The OLI sensor carried on Landsat-8 has eight multispectral channels with a spatial resolution of 30 m, and the central wavelengths are 443 nm, 483 nm, 561 nm, 655 nm, 865 nm, 1609 nm, and 2201 nm. Compared to its predecessors it has narrower bandwidth, much higher SNR (166–450), and 12-bits radiometric resolution. The Sentinel-2 satellites, S2A and S2B, are part of the Copernicus Programme (European Commission and European Space Agency) and were launched in 2015 and 2017, respectively. They carry the MSI sensor that has spatial resolutions of 10 m, 20 m, and 60 m in different bands, an SNR range of 50 to 174, and a radiometric resolution of 12 bits.

L8/OLI and S2/MSI were designed for land studies, but their improved radiometric resolution and SNR allow their use for water (e.g., Franz et al. [28,64]; Pahlevan et al. [65]). The much finer spatial resolution compared to other ocean color missions such as MERIS, and MODIS may be particularly useful for remotely monitoring lakes and reservoirs with a small surface area. The Level-1 TOA reflectance products, which have been radiometrically calibrated, corrected, and geo-referenced, were downloaded from Google Cloud Storage (GCS) (gs://gcp-public-data-{mission}).

2.4. In Situ Data Processing and Quality Control (QC)

2.4.1. C-OPS

The C-OPS (see full description in Morrow et al. [61] and Hooker et al. [66]) is a free-falling instrument that measures vertical profiles of downwelling irradiance (E_d, μW/(cm^2 nm)) and upwelling radiance (L_u, μW/(cm^2 nm sr)) in the water column in 19 wavebands at 15 Hz. The above-surface downward irradiance $E_d(0^+)$ was also measured simultaneously with a radiometer attached on top of the boat making sure that no obstructions were in the field-of-view. The in-water vertical profile of upwelling irradiance E_u(μW/(cm^2 nm)) can also be measured by deploying an extra sensor on the profiling unit. In the LakePulse fieldwork campaign, four C-OPS instruments (labeled as A, B, C, and D) with different waveband settings were used. The waveband settings of each instrument are provided in the Supplementary Materials (S1). The wavebands range from UV to NIR with the shortest and longest wavebands being 320 nm and 875 nm, respectively. The sensor for measuring E_u was only available on C-OPS B and allowed an assessment of the Q-factor (sr), i.e., the ratio of upwelling irradiance to radiance ($E_u(0^-)/L_u(0^-)$ [67].

Three to five light profiles were performed with the C-OPS at each station (one station per lake). The boats were either drifting during the measurements due to wind dragging or maintained outside the light field using the boat engine, making sure the instrument was kept outside any disturbance or boat shadow. To reduce the influence of the shadow from the instrument itself, the operator dropped it perpendicular to the direction of the sunlight.

The data were processed in the R software with the Cops package developed by B. Gentili at the Laboratoire d'Océanographie de Villefranche (LOV) and maintained by S. Bélanger (the source code is available at https://github.com/belasi01/Cops, accessed on 20 November 2019). The data processing follows the NASA protocols [68]. R_{rs} was derived from vertical profiles of $E_d(z)$, $L_u(z)$ and when available, upwelling irradiance $E_u(z)$. Each profile was carefully inspected and records showing instrument tilt greater than 10° were discarded for both in-water and above surface sensors. For each profile, the near-surface measurements were excluded because of the noise caused by the wave focusing effects under a clear sky. A LOESS regression was used to smooth the profile measurement and a linear regression on log-transformed data was used to extrapolate $L_u(z)$ and $E_u(z)$ to the water-air interface below the water, $L_u(0^-)$ and $E_u(0^-)$, respectively. Although the instrument was operated to reduce the influence of the shadow, some instrument self-shading is inevitable. The self-shading correction method based on absorption coefficient (Gordon and Ding, 1992; Zibordi and Ferrari, 1995) was used to correct $L_u(0^-)$ and $E_u(0^-)$. The total absorption coefficient was estimated using the measured reflectance and diffuse attenuation of downwelling irradiance following Morel and Maritorena [69] (their Equation (8)). The $L_u(0^-)$ was further transformed to $L_u(0^+)$ using Equation (1), referred to as water-leaving radiance L_w.

$$L_w(\lambda) = 0.54 L_u\left(0^-, \lambda\right) \tag{1}$$

where, the factor 0.54 accounts for the partial reflection and transmission of the upwelled radiance through the sea surface [68]. Thus, remote sensing reflectance R_{rs} for each profile was then calculated using Equation (2):

$$R_{rs}(\lambda) = L_w(\lambda)/E_d\left(0^+, \lambda\right) \tag{2}$$

Once each profile for a given station was processed, all the C-OPS profiles for the station were compared. Spectra that differed strongly (amplitude or shape) from the others were discarded. The remaining spectra were averaged to obtain the final R_{rs} spectrum. In addition, the Q-factor for each C-OPS channel was calculated for 71 stations in total (Figure 4) and used in the processing of the in-water measurements obtained with the HyperOCR irradiance sensor (Section 2.4.4). Larger variations in the spectral end members (UV and NIR) indicate larger uncertainty in the Q-factor due to a lower absolute signal in L_u and E_u and stronger vertical attenuation in these spectral ranges.

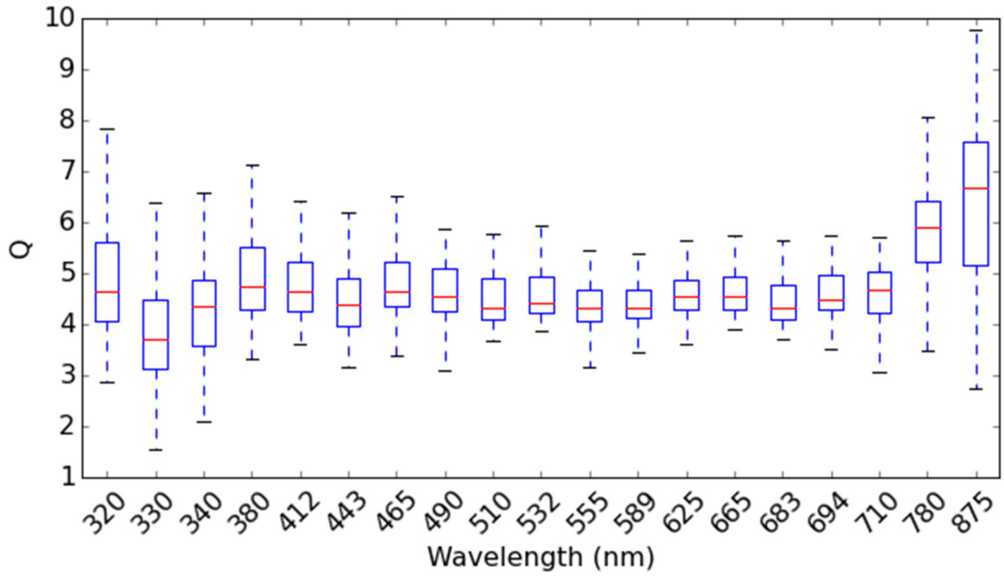

Figure 4. Statistics of the Q factor measured by C-OPS.

2.4.2. Analytical Spectral Device (ASD)

The above-water hyperspectral R_{rs} was determined using handheld portable spectroradiometers (ASD FieldSpec Pro) with a spectral range between 350 and 1050 nm and a spectral resolution of 1 nm. The measurements were made between 90 and 135° azimuthal angle relative to the position of the Sun and at a 30° to 40° nadir angle relative to the vertical to minimize sun glint [70]. At each site, the upward radiance above the water surface ($L_{tot}(0^+, \lambda)$), which includes water-leaving radiance and the reflected sky radiance, sky radiance ($L_{sky}(0^+, \lambda)$), and the radiance of a standard grey or white panel (L_p) were measured, and the measurements were repeated at least 10 times. Viewing geometry, wind speed, wind direction, and weather conditions were also recorded for auxiliary analysis.

The data were processed in R with the open-source ASD package developed by Simon Bélanger (https://github.com/belasi01/asd, accessed on 20 November 2020). Finally, R_{rs} was calculated using Equation (1), water-leaving radiance L_w and downwelling irradiance above water surface E_d were calculated using Equations (3) and (4), respectively.

$$L_w(\lambda) = L_{tot}(\lambda) - rL_{sky}(\lambda) \tag{3}$$

$$E_d\left(0^+,\lambda\right) = \left(\pi L_p(\lambda)\right)/\rho_p \tag{4}$$

where, r refers to the reflectance of the skylight at the water-air interface, for a cloudy sky ($L_{sky}(0^+,750)/E_d(0^+,750) \geq 0.05$), r is given a constant value of 0.0256 [71], otherwise, r is interpolated from Mobley's LUT [70] for the actual sun-viewing geometry and the wind speed, ρ_p refers to the reflectance of the white or gray board, obtained from the calibration process. The values of r predicted from these models hold true in general but are often suboptimal for individual measurements taken under continuously changing conditions (wave and ship motion, illumination) [72]. Therefore, the preliminary calculated R_{rs} needed to be further checked and corrected for the errors caused by non-perfect r and residual sky glint or sun glint contaminations. In the ASD R package, a variety of methods that are based on nil radiance assumption for specific bands, i.e., NIR and UV [73,74], the similarity spectrum [71], and synchronic C-OPS measurement are available. The method based on simultaneous C-OPS measurement forces the ASD-derived R_{rs} to pass through the C-OPS R_{rs} at two wavelengths (second shortest and longest, respectively), and this method was the default when the simultaneous C-OPS measurements are available. Otherwise, the correction method was determined by the water conditions that were judged by the pictures taken at the time of sampling, i.e., the method based on the similarity spectrum is used when the water is turbid, the UV nil radiance assumption (~350 nm) [73] was used when the water was rich in colored dissolved organic matter (CDOM) and low in turbidity.

2.4.3. TriOS-RAMSES

An in-water TriOS-RAMSES system consists of two hyperspectral radiometers with a sampling interval of approximately 3.3 nm and an effective spectral resolution of about 10 nm covering the spectral range 318–950 nm. One sensor was used to collect the upwelling radiance just below the water surface $L_u(0^-)$, while the second radiometer simultaneously recorded the downward irradiance $E_d(0^+)$ just above the water surface. The system was deployed at the sun incidence side of the boat to minimize ship shadow. The data were processed using a Python script developed by the Laboratoire d'Océanologie et de Géosciences (LOG) in France. R_{rs} was calculated using Equations (1) and (2), $L_u(0^-)$ and $E_d(0^+)$ were filtered according to the 25th and 75th percentile of the measurement at 490 nm before the averages were taken. Note that the upwelling radiance was measured at about 4 cm below the water surface, and it was assumed to approximately represent the $L_u(0^-)$ without accounting for the effect of the top ~4 cm, leading to a slight underestimation of the R_{rs}.

2.4.4. HyperOCR

Similar to the above setup, two hyperspectral ocean color radiometers (HyperOCR, Satlantic) were configured to measure the in-water upwelling irradiance just below the water surface $Eu(0^-)$ and in-air downward irradiance $Ed(0^+)$. The radiance is measured at about 3 nm increments from 380 to 800 nm. In addition, each spectral band is approximately 10 nm wide. The sensor measuring $E_u(0^-)$ was placed about 5–10 cm below the water surface. The data were processed in R using the open-source HyperOCR package developed by Simon Bélanger (https://github.com/belasi01/HyperocR, accessed on 20 November 2019). The reflectance R just below the water surface was calculated using Equation (5):

$$R(0^-,\lambda) = E_u(0^-,\lambda)/\left[0.96E_d(0^-,\lambda)\right] \quad (5)$$

R_{rs} was further calculated using Equation (6) (Lee et al. [75]):

$$R_{rs}(\lambda) = 0.52R(0^-,\lambda)/\left(Q - 1.7R(0^-,\lambda)\right) \quad (6)$$

where, Q refers to the Q factor, in general, its value ranges between 3 and 6 in the nadir direction [67]. In this study, the median Q factor (~4) measured by the C-OPS (Figure 4) was adopted to calculate R_{rs} for the HyperOCR.

2.4.5. Database of R_{rs}

For each station, there may be more than one R_{rs} measurement from the different instruments described above, but only one measurement was kept. Since the C-OPS measurements have been well-calibrated and each vertical profile verified, they were used as the reference. When hyperspectral measurements (Trios RAMSES, HyperOCR, or ASD) deviated from C-OPS, the C-OPS measurements were used, when they agreed, the hyperspectral measurements were used. If C-OPS was not available, the hyperspectral measurement was adopted. Then, all R_{rs} measurements were linearly interpolated to a 1 nm interval from 410 nm to 875 nm. In order to validate the sensor-derived spectra, the hyperspectral R_{rs} with 1 nm interval was then converted to the sensor (L8/OLI, S2A/MSI, and S2B/MSI) equivalent R_{rs} based on the sensor's relative spectrum response.

2.5. Atmospheric Correction Algorithms and Evaluation

When formulated in terms of planetary reflectance ρ (Equation (7)) instead of radiance L,

$$\rho = \frac{\pi L}{F_0 \cos\theta_0} \quad (7)$$

where F_0 is the extraterrestrial solar irradiance, and θ_0 is the solar zenith angle, the observation of satellite sensor at TOA over inland waters ρ^{TOA} can be expressed as in Equation (8) considering adjacency effects in general:

$$\rho^{TOA} = \rho_R + \rho_A + T\rho_{sg} + T\rho_g + t\rho_{wc} + t\rho_w + \rho_{adj} \tag{8}$$

where, the subscripts R, A, g, sg, wc, w, and adj refer to the Rayleigh scattering, aerosol scattering including multiple scattering with molecular, the reflectance due to the reflection of skylight by the water surface (skyglint), sun glint, white cap, water column, and adjacency effects, respectively, t and T refer to the diffuse and direct transmittance in the sea surface-to-sensor direction. AC is generally considered as the procedure of removing all the items in the right part of Equation (8) to derive ρ_w. It is worth clarifying that: (1) most AC processors do not include the removal ρ_{adj}; (2) different AC processors may adopt different parametrization of the terms in Equation (8), e.g., the NASA level-2 generator (l2gen), ρ_{sg} is included in the lookup tables of ρ_R and ρ_A; (3) very likely in AC processors developed to process land images ρ_R and ρ_A are for sole atmospheric scattering (i.e., the atmosphere is bounded by an absorbing surface) and consequently they do not include the skyglint contribution. Seven AC processors were evaluated in this study (Table 1): l2gen (V7.5.1), ACOLITE (V20190326.0), the Landsat 8 Surface Reflectance Code (LaSRC), Sen2Cor (V02.08.00), ICOR (V1.0), the Case 2 Regional Coast Colour processor (C2RCC, V1.0) and the POLYnomial based algorithm (POLYMER, V4.12). LaSRC and Sen2Cor were designed for L8/OLI and S2/MSI, respectively, while the other processors can handle both L8/OLI and S2/MSI (Table 1). In some of the processors, more than one algorithm or model is implemented. As a result, a total of ten configurations were tested (Table 1). NASA's l2gen processor was run in both the NIR-based standard algorithm (hereafter STANDARD) [76,77] and the SWIR-based black pixel algorithm (hereafter SWIR) [78]. The STANDARD algorithm adopts an iterative scheme that is based on the 'black pixel' assumption and a priori, known NIR water-leaving radiance model.

The ACOLITE processor, which has been developed at the Royal Belgian Institute of Natural Sciences (RBINS) for aquatic applications of Landsat series and Sentinel-2 (A/B) satellite data, includes the default Dark Spectrum Fitting (DSF) algorithm [40,79]. The DSF computes atmospheric path reflectance based on multiple dark targets in the scene or subscene with no a priori defined dark band. For each band, the darkest object is estimated from the offset of an Ordinary Least Square (OLS) fit to the first thousand pixels in the histogram and aerosol model; aerosol optical thickness (AOT) at 550 nm is estimated based on the darkest object. In this study, only the recommended DSF algorithm was evaluated.

LaSRC was developed by NASA/USGS for the atmospheric correction of Landsat-8 for terrestrial application. It calculates and removes the aerosol contribution from the TOA reflectance using auxiliary data, such as AOT, water vapor, and ozone retrieved from MODIS imagery, and digital elevation derived from GTOPO5, as the inputs of its internal radiative transfer model [80]. Although the processor is not publicly accessible, its surface reflectance products were obtained from Google Earth Engine (GEE) and the USGS Earth Explorer.

Sen2Cor is the ESA standard atmospheric correction processor for S2/MSI which was developed for land application [42]. It estimates the AOT at 550 nm using the Dense Dark Vegetation (DDV) algorithm based on the scene classification results. The algorithm requires that the scene contains reference areas of known reflectance behavior, preferably DDV and/or dark soil and/or water bodies. If the scene contains no DDV pixels, constant AOT which is specified in the configuration file will be used. When Sen2Cor is used for water application, the AOT estimated over land pixels in the image is used for the water surface, but the water surface effects such as sun and sky glint are neglected [42]. Aerosol reflectance is then calculated and removed based on the libRadtran LUTs [81]. In addition, AE correction is also included in the processing procedure. The AE correction algorithm is based on the model proposed by Richter [53] (hereafter RICHTER1990). Briefly, this model estimates the TOA reflectance due to AE by calculating the reflectance difference between the target pixel and its surrounding environment (default is 2 km), it was implemented in ATCOR [82] and Sen2Cor integrated this implementation. The Sen2Cor processor is available as a third-party plugin of the Sentinel-2 Toolbox (SNAP).

Table 1. List of the AC algorithms used to process L8/OLI and S2/MSI images in this study.

Algorithm	Processor	Description	AE Correction	Strategy of R_{rs} Retrieval
SWIR [78]	l2gen in SeaDAS (V7.5)	Black pixel assumption based on two SWIR bands	NO	R_{rs} is retrieved through estimating and removing aerosol attribution
STANDARD [76,77]		An iterative scheme based on black pixel assumption a priori known NIR water-leaving radiance	NO	
ACO_DS [40,79]	ACOLITE (V20190326.0)	Dark Spectrum Fitting (DSF)	NO	
LaSRC [80]	LaSRC	L8/OLI only The processor that generates R_{rs} for GEE	NO	
Sen2Cor [42]	Sen2Cor (V02.08.00)	S2/MSI only, ESA standard AC algorithm for S2/MSI	RICHTER1990	
ICOR [41]	ICOR in SNAP (V7.0)	Land-based aerosol estimation for inland waters	NO	
ICOR_SM [49]		Same as ICOR, but the adjacency effects correction algorithm is integrated.	SIMEC	
C2RCC [37,38]	C2RCC in SNAP (V7.0)	NN-based, the model is trained based on simulated datasets for Case-2 water	NO	R_{rs} is retrieved directly through optimizing a coupled atmosphere-water system.
C2X [38]		NN-based, the model is trained based on simulated datasets for extremely Case-2 waters	NO	
POLYMER [39]	POLYMER (V4.12)	Spectral optimization	NO	

ICOR, previously known as OPERA [83], is a processor that performs atmospheric correction based on the MODTRAN LUTs. ICOR can handle both land and water targets. AOT is estimated based on an adapted version of the algorithm developed by Guanter [84] from land pixels. Correction of adjacency effect (AE) for land and water bodies is included in ICOR as an option. For land, AE is applied with a fixed range, while over water the SIMilarity Environmental Correction (SIMEC) algorithm [49], which estimates the contribution of the background radiance based on the correspondence with the Near-InfRared (NIR) similarity spectrum, was implemented. To make a comparison, both ICOR with and without the AE correction (ICOR_SM) were tested in this study.

The atmospheric correction algorithms STANDARD, SWIR, ACO_DS, LaSRC, Sen2Cor, ICOR, and ICOR_SM described above, all adopt the same strategy of estimating and removing the aerosol reflectance, although the aerosol reflectance estimation methods are different. However, C2RCC [38] and POLYMER [39] (Polymer atmospheric correction algorithm Issue: 2.1, 2016) do not. Instead, they adopt a coupled atmosphere-water model and optimization technique strategy, and the aerosol optical properties and water reflectance or R_{rs} are solved simultaneously by optimizing an objective function. The main difference is that C2RCC uses a neural network for the optimization while POLYMER uses a nonlinear optimization technique. In the C2RCC processor, two neural network (NN) models, the C2RCC and C2X Nets, which were trained using the Case-2 and Case-2 extreme waters dataset, respectively, are available and tested herein. Altogether, it resulted in ten AC processing configurations (Table 1).

2.5.1. Specific Processing Steps

Most of the default algorithms settings were kept for processing the images, however, some were modified due to the context of this study. The key options chosen are described in Table 2. For SWIR and STANDARD, the outband_opt option was set to 0 to ignore the transformation to nominal wavelength. In addition, to reduce the processing time, only a subscene of 0.05° by 0.05° (approximately 5.6 km by 3.7 km near the latitude of 48°) centered at the sampling station was processed. The two bands for aerosol estimation were set as 1609 (1613) and 2201 (2200) nm when the SWIR algorithm was used to process L8/OLI (S2/MSI). For STANDARD, the two bands were set as 865 nm and 1609 nm for L8/OLI, and 865 nm and 1613 nm for S2/MSI. For the DSF algorithm in ACOLITE, a fixed or a tiled path reflectance is optional, in this study, a fixed path reflectance with a subregion of 0.05 degree by 0.05 degree centered at the sampling was chosen. For ICOR and ICOR_SM, the window size for aerosol retrieving was set at 1000 by 1000 pixels which allowed more chance of a successful retrieval than the default 500 by 500 pixels setting. Except for ICOR, outputs of all the processors were resampled to the same spatial resolution of 20 m for all of the bands of S2/MSI although the L1 image has three different resolutions (10 m, 20 m, and 60 m). The outputs of ICOR have the same spatial resolution as the L1 image.

Table 2. Specific options of nine water-specific AC algorithms for L8/OLI and S2/MSI image processing. LaSRC options are not listed, the R_{rs} spectra were obtained directly from GEE instead of processing the L1 images of L8/OLI.

Algorithm	Common Options	Specific Options for L8/OLI	Specific Options for S2/MSI
SWIR	maskland = off east = lon + 0.025 west = lon − 0.025 north = lat + 0.025 south = lat + 0.025 outband_opt = 0	aer_swir_short = 1609 aer_swir_long = 2201	aer_swir_short = 1613 aer_swir_long = 2200
STANDARD	Same as SWIR	aer_wave_short = 865 aer_wave_long = 1609	aer_wave_short = 865 aer_wave_long = 1613
ACO_DS	dsf_path_reflectance = fixed dsf_spectrum_option = dark_list limit = lat − 0.025, lon − 0.025, lat + 0.025, lon + 0.025	NA	S2_target_res = 20
Sen2Cor	Default	NA	resolution = 20
ICOR	aot_window_size = 1000	NA	NA
ICOR_SM	aot_window_size = 1000 smiec = true	NA	NA
C2RCC	PnetSet = C2RCC	PvalidPixelExpression = "near_infrared > 0 and near_infrared < 100"	PvalidPixelExpression = "B8 > 0 && B8 < 0.5"
C2X	PnetSet = C2X-Nets	Same as C2RCC	Same as C2RCC
POLYMER	Default	NA	resolution = 20

2.5.2. Preparation of Matchups

Some studies have demonstrated successful matchups using less restrictive time interval windows between image collection and ground observation of R_{rs} of up to 3 days in lakes under stable hydrologic and atmospheric conditions [23,85–87]. In this study, the time window was set to eight days (i.e., in situ date ± 8 days) to obtain more matchups. The 8 days window is riskier for the validation when compared to the usual choice of 2 days or 30 h, more chance of extreme conditions that drastically changes the optical properties of the lakes could happen, e.g., strong winds or rainstorm. This can be detected by visual inspection of images and photographs taken during the measurement, for example, if the imagery shows clear water (dark blue), but the photo indicates turbid water, some extreme weather might have happened during the time window and this matchup was excluded. However, subtle changes cannot be detected this way. Considering the current cloud and cloud shadow detection algorithms are not perfect, cloud and cloud shadow was identified after a visual inspection of the natural-color RGB image generated from the TOA reflectance. Potential matchups were screened out when the pixels of the sampling station were contaminated by clouds or cloud shadows. However, images with very thin clouds (e.g., cirrus clouds) or haze were kept in this study to assess the capability of the current AC algorithms to handle this situation. Thus, the matchups were divided into three groups which contained all images (hereafter G-ALL), only the clear (hereafter G-CLEAR), and very thin cloudy (cirrus and haze) images (hereafter G-CIRRUS), respectively. Very few of the sampling stations were very close to the shore. The matchups with a minimum distance smaller than 90 m (i.e., 3 L8/OLI pixels) were excluded. A simple threshold method that the Rayleigh corrected reflectance in 865 nm < 0.1 was used to identify the water body. Note that the non-water pixels identified by the method in this study may also contain the cloudy pixels, therefore, this procedure also excluded the matchups contaminated much by adjacent clouds. To exclude a few measurements that might have been potentially affected by the bottom reflectance, the photos taken in the field were investigated visually.

To screen out the matchups that may be contaminated by sun glint, the Sun's specular reflectance was estimated using a script developed by Bailey (2014) based on the observation geometry of the satellite image pixel at the sampling station. The wind speed was set to 5 m/s if the measurement was not available. Potential matchups with an estimated normalized glint radiance greater than 0.005 were excluded.

2.5.3. Evaluation Metrics

In this study, we evaluate algorithm performance following Pahlevan et al. [34] to facilitate comparison to the recent ACIX-Aqua study and others. Three main metrics that focused on the error, bias, and the similarity of the spectrum shape were defined as Equations (9)–(11), respectively.

$$\text{Bias} = 100\,\text{sign}(Z)10^{|z|-1},\ \text{where } Z = \text{median}(\log_{10}\left(\frac{R'_{rs}}{R_{rs}}\right)) \tag{9}$$

$$\text{Error} = 100\left(10^{|Y|-1}\right),\ \text{where } Y = \text{median}\left|\log_{10}\left(\frac{R'_{rs}}{R_{rs}}\right)\right| \tag{10}$$

$$\text{SA} = \cos^{-1}\left(\frac{R'_{rs}\cdot R_{rs}}{||R'_{rs}||\ ||R_{rs}||}\right) \tag{11}$$

where, R_{rs} and R'_{rs} refer to in situ and satellite-derived remote sensing reflectance, respectively. Bias and Error represent the symmetric signed percentage bias and the median symmetric accuracy, respectively. Similarity Angle (SA), which is the angle (degree) between the two points in the n-dimension space (n is the number of R_{rs} bands), represents the similarity of the measured and satellite-derived R_{rs} spectrum.

In addition, some of the algorithms might fail in processing (no R_{rs} products were generated) or generate NaN or negative R_{rs} values in certain bands. In this study, as long as the derived R_{rs} spectrum has all valid values in VIS bands, it is taken into account for the calculation of the metrics, since the VIS bands are more important for the estimation of water constituents and most R_{rs} in NIR bands are very low that near zero, otherwise, it was referred to as 'failure'. Therefore, the number of valid matchups generated by a certain algorithm also reflects one aspect of its performance. This number was therefore used as a reference indicator to evaluate the performance of algorithms.

2.6. Radiative Transfer Simulations

We modeled the adjacency reflectance ρ_{adj} as Equation (12):

$$\rho_{adj} = \rho^{TOA} - \tilde{\rho}^{TOA} \quad (12)$$

where, ρ^{TOA} refers to the reflectance at the sensor originating from the target waterbody which includes the contribution from the land (i.e., the surrounding/adjacent environment), $\tilde{\rho}^{TOA}$ refers to the reflectance that would reach the sensor if the surface was all covered by the homogenous water. AE are estimated by the percent adjacency reflectance $\xi\rho_t$ at the sensor level (Equation (13)).

$$\xi\rho_t = \frac{\rho_{adj}}{\rho^{TOA}} * 100\% \quad (13)$$

The 3D Monte Carlo radiative transfer model MCARATS (v0.9.5) (Iwabuchi, 2006) was used to simulate ρ^{TOA} and $\tilde{\rho}^{TOA}$. To simplify the conditions of atmosphere and water, several assumptions were made:

- Physical properties of the atmosphere are horizontally homogeneous.
- Land surface are Lambertian and flat.
- Reflectance of the water body is spatially homogeneous.
- Reflectance of the water body includes two parts, the reflectance due to the water-leaving radiance and the water surface reflected diffuse downwelling irradiance.
- No wind over the lake, and the water surface is assumed to be Lambertian.

The NASA standard atmosphere profile of mid-latitude summer was used to calculate the extinction coefficient due to Rayleigh scattering and the total gas absorption. The inputs related to aerosol including the phase function, the single scattering albedo, and the angstrom coefficients were calculated based on the aerosol model developed by Ahmad [88] (hereafter referred to as Ahmad 2010) and adopted in the l2gen program. An arbitrary vertical distribution of aerosol concentration was chosen to calculate the extinction coefficient profile due to aerosol scattering for a given AOT.

AE were simulated for two different cases, one for an ideal scenario and another for a real case study. In the following table, we briefly describe the main inputs of the simulations (Table 3), and more details are available in the Supplementary Material (S2). For the ideal scenario, the shape of the lake was assumed to be a circle and the water relatively clear, and the surrounding land is assumed to be covered in homogenous green vegetation, the spectra are shown as Figure S3 in the Supplementary Material S2. Four different sizes of lakes with an area of 5, 20, 50, and 100 km^2 corresponding to a radius of 1.26, 2.52, 3.99, and 5.64 km, were simulated to analyze the impact of lake size on the adjacency effects. Five wavelengths corresponding to the center wavelengths of VIS and NIR of L8/OLI bands were simulated. Two AOT (0.07 and 0.2) were set to evaluate the effects of aerosol concentration on AE, the AOT of 0.2 was only applied to the area of 20 km^2. This is similar to the simulation of Santer [44] using 5S based on single scattering approximation and an exponential decay of the environment effect derived from the best fit of pre-existing MC simulations. It is worth mentioning that in addition to the presence of the atmosphere, the point spread function (PSF) of the sensor also reduces the contrast of the satellite image [89]. According to the PSF of the Enhanced Thematic Mapper Plus (ETM+), the distance affected by the PSF is around 60 m (2 pixels), and the further away from the pixel center, the weaker (see Figures 1 and 2 in [89]). Therefore, the effect of PSF is small relative to the atmosphere. For the real case simulation in this study, since the PSF data of L8/OLI was not found, a similar PSF ofETM+ was used instead. For the real case study, the Dragon Lake (central location, 122.414°W, 52.954°N; ID 11-631) located in British Columbia (BC, Canada) with an area of 0.44 km^2 is used as an example. The shape of the lake and the surface reflectance by the land were taken from the semi-synchronized S2/MSI image resampled to 30 m per pixel after AC by Sen2Cor, and the water-leaving reflectance was taken from the nearly synchronized measurement of station 11-631 (see Figure 5). The water body was identified using an experienced threshold of 0.06 for the surface reflectance at band 8 (843 nm). The value of AOT (550) was determined from the Sen2Cor-derived level-2 product. Note that in the two cases, the diffuse downwelling irradiance (skylight) that is reflected by the water surface was considered. The diffuse downwelling irradiance was simulated using Second Simulation of a Satellite Signal in the Solar Spectrum-Vector (6SV) and the reflectance of the skylight at the water-air interface r was simply set as 0.0256 to represent a water surface in the absence of wind (see Section 2.4.2). Therefore, the input of reflectance for water (ρ_s) is the sum of the reflectance due to the water-leaving radiance (ρ_w) and skyglint ρ_{sg} (Equations (14) and (15)),

$$\rho_s(\lambda) = \rho_w(\lambda) + \rho_{sg}(\lambda) \tag{14}$$

$$\rho_{sg}(\lambda) = r\frac{E_d(0^+, \lambda)}{F_0(\lambda)\cos(\theta_s)} \tag{15}$$

where, F_0 refers to the extraterrestrial irradiance. For the real case simulation, PSF was not applied, because the surface reflectance of all the bands with resolutions of 10 m, 20 m, and 60 m was resampled to 30 m, and this means it has been blurred for the bands with 10 m and 20 m resolution.

Table 3. Main inputs of the 3D simulation.

Parameters		Ideal Case	Real Case
Dimension		256 × 256 pixels	
Initial Photons		5×10^{10}	
Aerosol	AOT	AOT(865) = 0.070, 0.2	AOT(550) = 0.065
	Model & type	Ahmad2010 Relative Humidity (RH) = 70, Fine Mode Fraction (FMF) = 0	Ahmad2010 RH = 75, FMF = 95
	Vertical distribution	Arbitrary (see Figure S2 in Supplementary Material S2)	
Geometry		$\theta_s = 30°, \theta_v = 0°$	$\theta_s = 44.9°, \theta_v = 8.0°$ Relative azimuth $\phi = 118°$
Atmosphere profile		NASA standard, mid-latitude summer (see Figure S1 in Supplementary Material S1)	
Surface reflectance	water	Homogenous In situ Measurement (04-620) (see Figure S3 in Supplementary Material S2)	Homogenous In situ Measurement (11-631) (see Figure S4 in Supplementary Material S2)
	Land	Homogenous green vegetation (see Figure S3 in Supplementary Material S2)	Heterogeneous Sen2Cor derived surface reflectance (see Figure S4 in Supplementary Material S2)

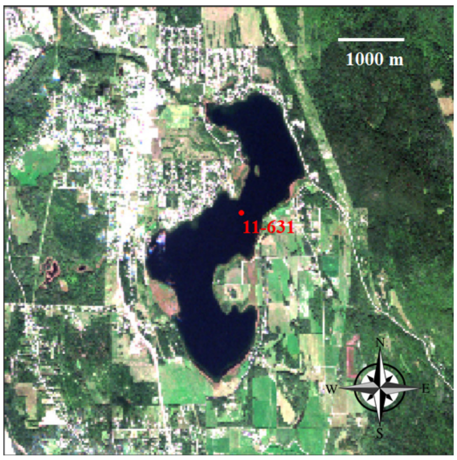

Figure 5. Natural color image of Dragon Lake from S2B/MSI (S2B_MSIL1C_20190829T190919_N0208_R056_T10UED_20190829T21). The location of the sampling station 11-631 is also shown.

3. Results

An example for the sampling site of 11-631 (see Figure 5) is given in Figure 6 to show the validation of AC algorithms using the in situ measurement. As shown, eight R_{rs} spectra are obtained from eight AC algorithms, the SWIR algorithm is not missing because of the failure. In addition, the STANDRAD only generates two valid values in two NIR bands, respectively, R_{rs} in the other bands are negatives. Surprisingly, POLYMER also generates negative values in two NIR bands, but valid values in the VIS bands. Except for C2RCC, C2X, and POLYMER, of which the forward water models always generate pretty much constant values in NIR bands, the other algorithms have significantly overestimated R_{rs} in NIR bands. However, the Rrs spectra in VIS bands derived by C2RCC, C2X, and POLYMER were much different and totally inconsistent with the measurement. According to the method described in Section 2.5.3, STANDRAD and SWIR are considered 'failures', but POLYMER is considered valid as well as the other algorithms. Statistics of the metrics and the results of the simulations are presented as follows.

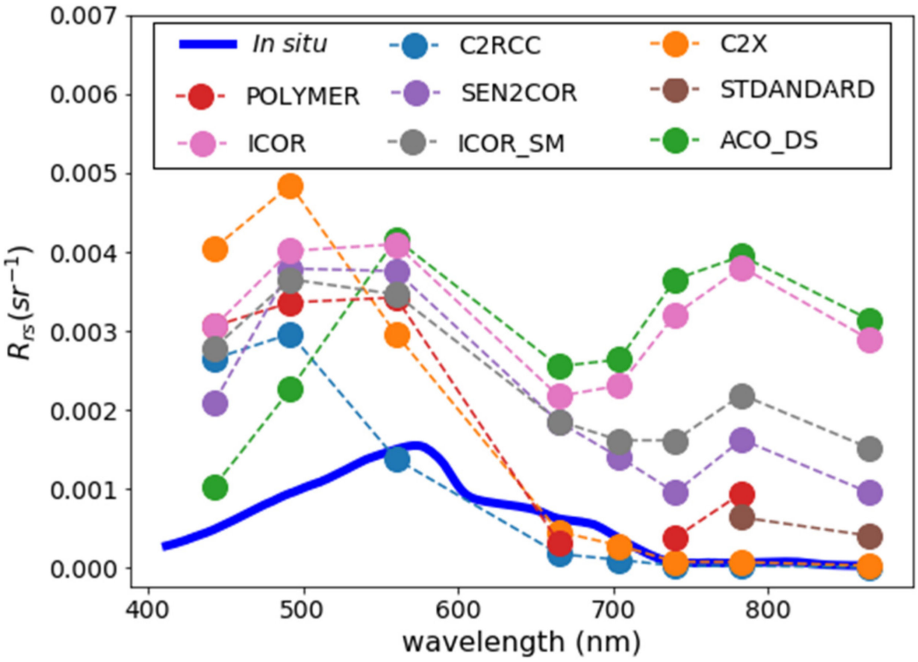

Figure 6. Comparison between the in situ R_{rs} measured by TriOS RAMSES (24 August 2019 18:38 UTC) and the R_{rs} retrieved by each algorithm for the sampling station of 11-631 from the Sentinel-2/MSI observation (29 August 2019 19:09 UTC). The measured Chla concentration was 1.55 µg/L.

3.1. Number of Valid Matchups

After applying the criteria and methods described above, we obtained in total 214 and 413 matchups for L8/OLI and S2/MSI, respectively. The number of matchups that failed in G-CIRRUS for L8/OLI and S2/MSI were 39 and 141, respectively. The distribution of the number of matchup pairs falling in different time windows is shown in Figure 7.

Table 4 shows the comparison of the numbers of valid matchups for each algorithm for L8/OLI and S2/MSI, respectively. As mentioned above, up to 214, and 413 matchups were found for a given processor for L8/OLI and S2/MSI. As listed, the STANDARD and SWIR algorithms have very few matchups for each band, which indicates that most of the water-leaving radiance retrieval has failed. Except for STANDARD and SWIR, the other algorithms have almost the same number of valid matchups, while C2RCC and C2X have no failures. Regarding failures, they appear in both groups of G-CLEAR and G-CIRRUS, indicating that the related algorithms failed not only for thin cloudy images but also for clear sky images.

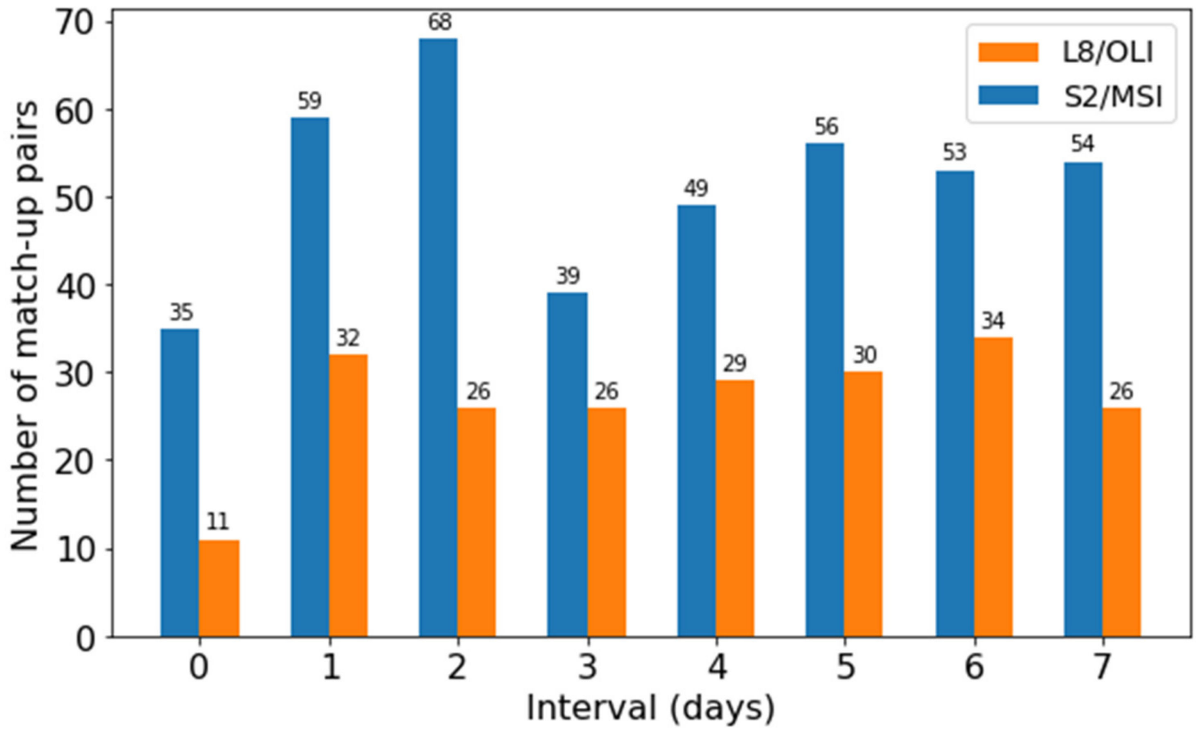

Figure 7. Distributions of the maximum matchups for L8/OLI and S2/MSI in each interval (days).

Table 4. Number and percentage of valid matchups for each algorithm.

	S2/MSI		**L8/OLI**	
	Number	**Percentage (%)**	**Number**	**Percentage (%)**
STANDARD	17	4.1	4	1.9
SWIR	6	1.5	1	0.5
ICOR	380	92.0	201	93.9
ICOR_SM	326	78.9	181	84.6
C2RCC	413	100	214	100
C2X	413	100	214	100
POLYMER	236	57.1	203	94.9
LaSRC	NA	NA	183	85.5
ACO_DS	376	91.0	206	96.3
SEN2COR	382	92.5	NA	NA

3.2. Validation of Remote Sensing of Reflectance

This section presents the performance of the selected AC for L8/OLI (Section 3.2.1) and S2/MSI (Section 3.2.2). The evaluation metrics of Bias and Errors were calculated for each visible band and algorithm. The SA were also calculated for each algorithm. STANDARD and SWIR were excluded from this evaluation as there are too few valid matchups resulting in meaningless statistics. The metrics were also calculated for matchups in each group (G-ALL, G-CLEAR, and G-CIRRUS).

3.2.1. L8/OLI

Figure 8 shows the performance of each algorithm for L8/OLI in terms of Bias, Errors, and SA only for G-ALL and G-CIRRUS groups as G-CLEAR are very similar to those of G-ALL due to a similar number of matchups. The magnitudes of Bias and Errors reach hundreds of percent, which are much higher than the results reported in other comparison exercises (e.g., Pahlevan et al. [34]), however, huge differences also exist between algorithms. Focusing on the G-ALL group (upper panels in Figure 8) in terms of Bias and Errors, the values of C2RCC and C2X, which have similar results, are lower than other algorithms.

The other algorithms show similar but much higher values. This difference is particularly strong in the blue band, which is most affected by atmospheric scattering including aerosol, where Bias and Errors of C2RCC and C2X are much lower than in others. However, the values still reach an unacceptably high value of around 200%. It is worth noting that only the Bias of C2RCC and C2X in B4 is negative (underestimation of L_w), while others are all positive (overestimation). The positive Bias leads to similar results for Errors shown in the middle panels. In terms of bands, the B3 (560 nm) has the lowest Errors for all the algorithms. Although C2RCC and C2X outperform other algorithms in terms of Bias and Errors in each individual band, this is not the case in terms of SA (the right panels in Figure 8). The median SA of C2RCC and C2X is only lower than POLYMER, but higher than other algorithms. The lowest median SA (18) was returned by ACO_DS, which implies that ACO_DS has the best performance in preserving the spectral shape, but not the magnitude.

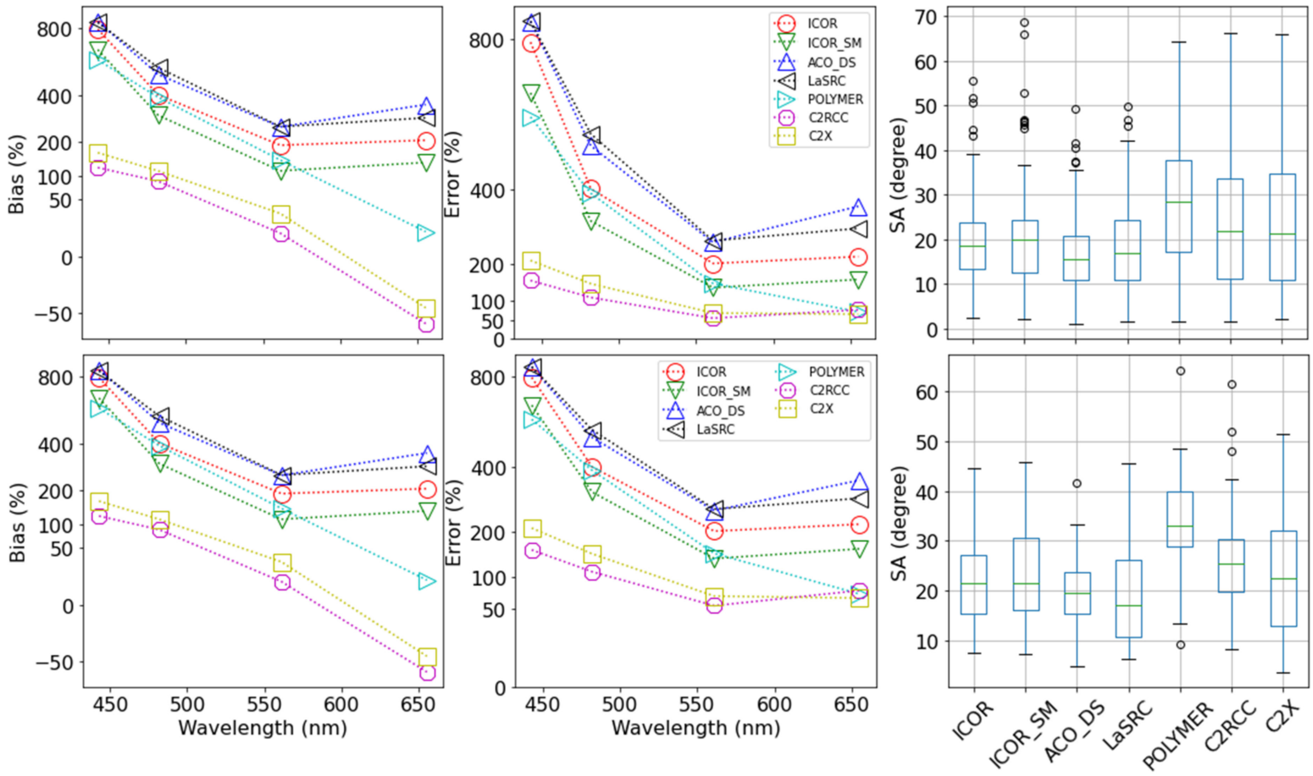

Figure 8. Performance assessment of the processors in terms of median bias (left), errors (middle), and similarity angle (right) for the G-ALL (upper) and G-CIRRUS group (bottom), respectively, for Landsat 8. In the boxplots, the median values are shown as the green lines, and the circles represent the outliers.

Considering the number of matchups for the B5 band (865 nm) is much lower because of the absence of the NIR bands for some in situ sensors (e.g., HOCR), the evaluation of individual matchups is less meaningful. Therefore, a comparison of the statistics between the in situ dataset and the retrievals is made instead of matchups (Figure 9). The median R_{rs} retrieved by ICOR, ICOR_SM, ACO_DS, and LaSRC are much higher than that of the measurements (Figure 9), the relative differences reach approximately 10,000%, indicating these algorithms strongly overestimate $R_{rs}(865)$. Compared with ICOR, ICOR_SM, ACO_DS, and LaSRC, POLYMER, C2RCC, and C2X-derived R_{rs} have values that are much closer to that of the measurements even though the medians are a little lower than the measurements.

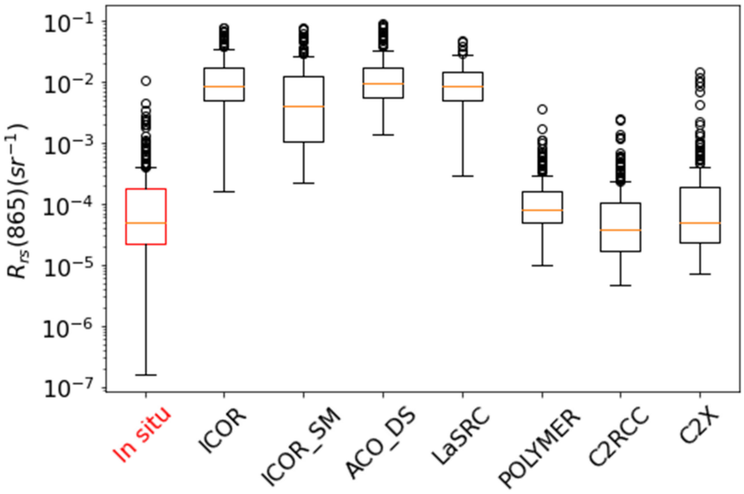

Figure 9. Comparison of the distributions of the in situ measured R_{rs} and R_{rs} retrieved by each processor in the NIR band (865 nm) of OLI (Landsat 8). The median values are shown as the green lines, and the circles represent the outliers.

3.2.2. S2/MSI

The same analyses were performed for S2/MSI (Figures 9 and 10). Overall, S2/MSI shows similar results as L8/OLI, but with higher Bias and Errors suggesting that the algorithms have worse performance for this sensor (Figure 10). C2RCC and C2X again outperformed other algorithms in B1 (443 nm) and B2 (490 nm), but their very low negative Bias and relative high Errors in B4 (665 nm) indicate a severe underestimation in the red band. In terms of SA, again ACOLITE outperforms others while C2RCC and C2X are the two worst. Some interesting results are found in terms of the matchup groups, except for C2RCC and C2X, the other algorithms have similar trends of higher, medium, and lower errors G-ALL (the upper panel in Figure 11) and G-CIRRUS (the bottom panel), respectively, while C2RCC and C2X have the similar errors for G-ALL and G-CIRRUS. This suggests that C2RCC and C2X are less sensitive to thin clouds than the others.

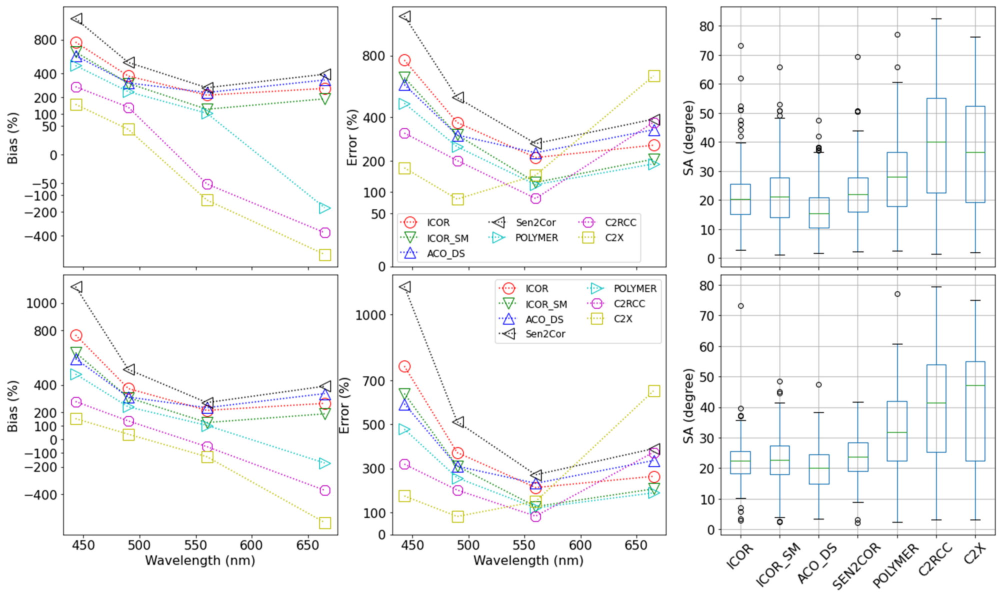

Figure 10. Performance assessment of the processors in terms of median bias (left), errors (middle), and similarity angle (right) for the G-ALL (upper) and G-CIRRUS group (bottom), respectively, for S2/MSI. In the boxplots, the median values are shown as the green lines, and the circles represent the outliers.

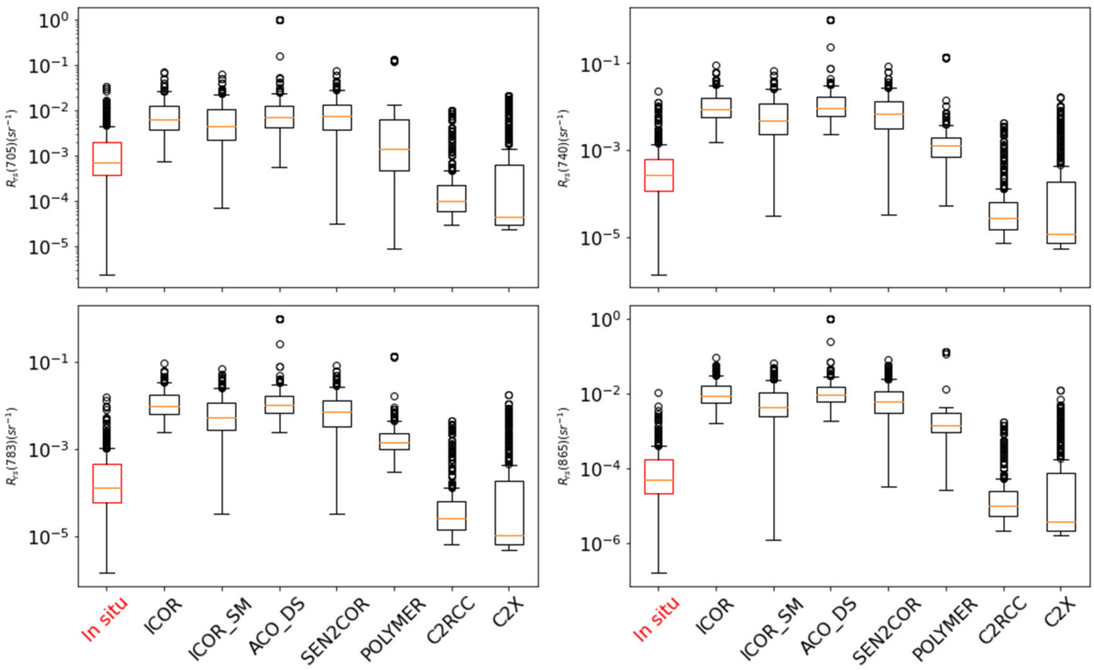

Figure 11. Comparison of the distributions of the in situ measured R_{rs} and R_{rs} retrieved by each processor in the NIR bands (705 nm, 740 nm, 783 nm, and 865 nm) for S2/MSI. The median values are shown as the green lines, and the circles represent the outliers.

Large differences between measured and retrieved R_{rs} are also found for the four NIR bands of S2/MSI (Figure 11). From the median R_{rs} shown in Figure 11, C2RCC and C2X-derived ones are lower than the measurements while they are higher for the other algorithms. Overall, compared with other algorithms, the differences related to C2RCC, C2X and POLYMER are lower, especially in the longest NIR band (865 nm).

3.3. Simulations of Adjacency Effects

3.3.1. Idealized Case

The adjacency reflectance ρ_{adj} was calculated based on the simulation of ρ^{TOA} and $\tilde{\rho}^{TOA}$. Figure 12 shows ρ_{adj} images at 865 nm and 655 nm for different lake areas. The smaller size of the lake, the greater ρ_{adj} is, indicating the stronger adjacency effects. Although there is more noise is at 655 nm than at 865 nm, which was caused by same the initial amount of photons used and the stronger extinction of the atmosphere at 655 nm (more photons will reduce the noise but will require much more time), we can also see clearly that $\rho_{adj}(865)$ is approximately 10 times greater than $\rho_{adj}(655)$, for the same lake size. For comparison, the surface land (vegetation) reflectance (ρ_s) used as input in the simulations was around 5 times higher at 865 nm relative to 655 nm (see Supplemental Materials S2). The ρ_{adj} approximately doubles for a lake with an area of 20 km^2 when the AOT increases from 0.07 to 0.2. It also shows that the closer the pixel is to the perimeter boundary the greater ρ_{adj}. To see the pattern clearly, the transect profiles from the boundary to the center of the lake are plotted (Figure 13). In addition to ρ_{adj}, the percent adjacency reflectance $\xi\rho_t$ and the ratio of ρ_{adj} and ρ_w are plotted as well. In general, an exponential decreasing value of $\xi\rho_t$ is found with distance to shore which agrees with other reports [51,54] and the slopes of smaller lakes were higher than larger lakes, such that the impact is not only lower but also decreases faster with distance from shore. Although the pattern was similar at 655 nm, there was also greater noise and lower magnitude. The strongest AE was found at 865 nm near the boundary for the smallest lake, and the ρ_{adj}, $\xi\rho_t$ and the ratio of ρ_{adj} and ρ_w exceed 0.015, 40% and 80%, respectively.

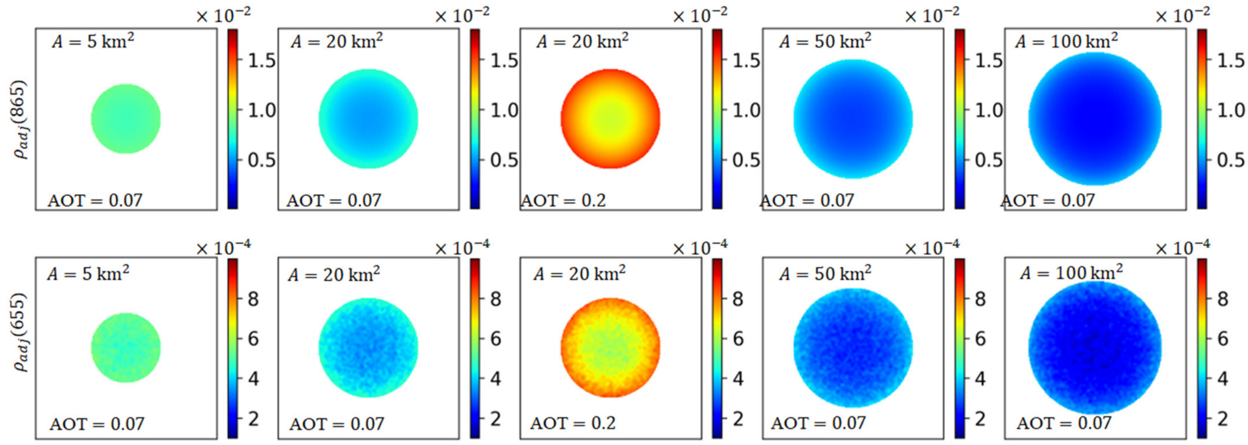

Figure 12. Images of the percent adjacency reflectance $\xi\rho_t$ in 865 nm and 655 nm for lakes with an area of 5 km^2, 20 km^2, 50 km^2, and 100 km^2. The letter A here represents the area.

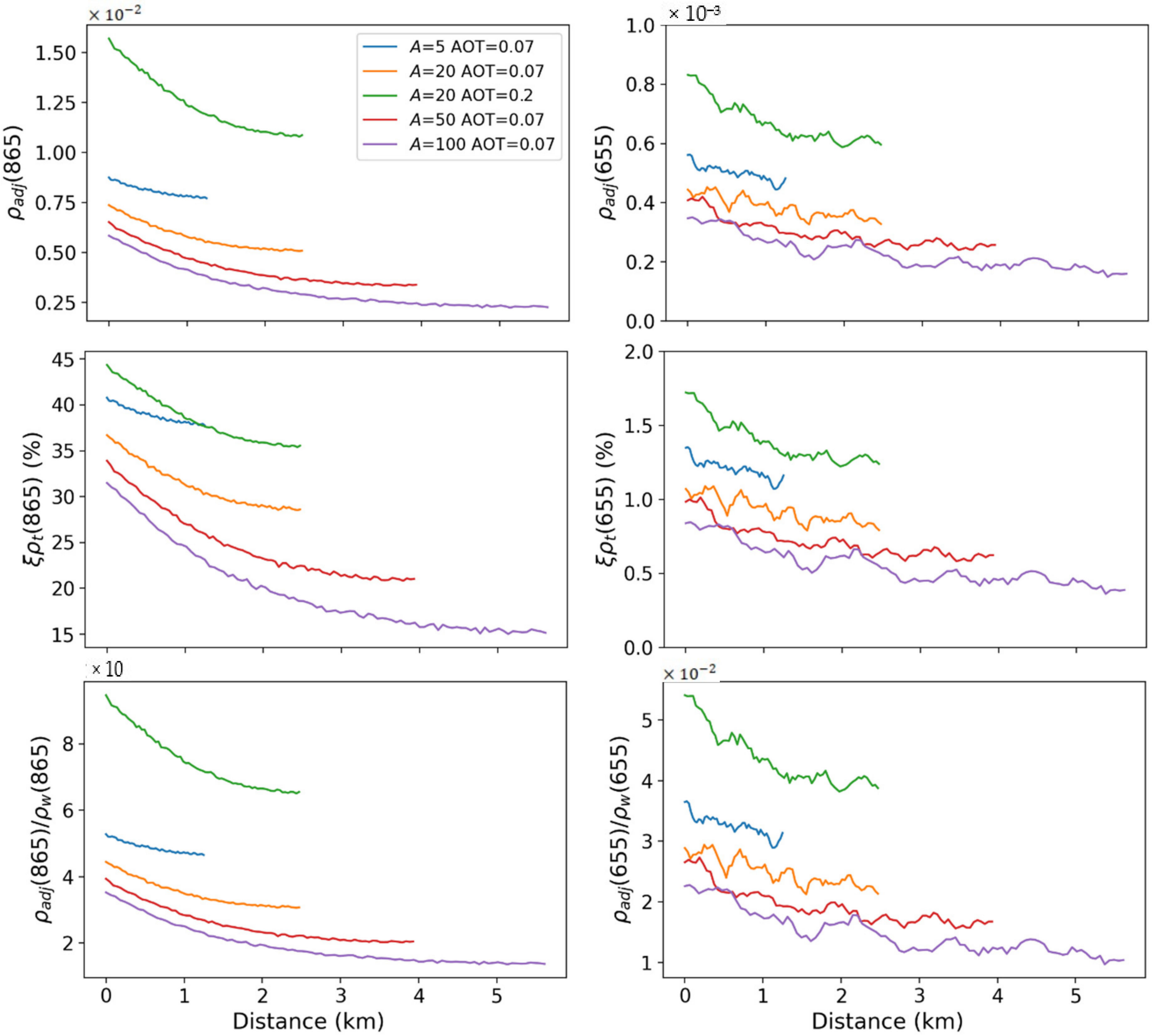

Figure 13. Transect (along a radius) of the adjacency reflectance ρ_{adj} (upper), the percent adjacency reflectance $\xi\rho_t$ (middle), and the ratio of ρ_{adj}/ρ_w (bottom) at 865 nm (left) and 655 nm (right) for hypothetical circular lakes with areas of 5 km^2, 20 km^2, 50 km^2, and 100 km^2.

3.3.2. Real Case

The simulated and satellite-observed TOA reflectance (ρ_{si}^{TOA} and ρ_{ob}^{TOA}), and their ratio ($\rho_{si}^{TOA}/\rho_{ob}^{TOA}$) for Dragon Lake (British Columbia, Canada) are shown in Figure 14. As shown, ρ_{si}^{TOA} agrees very well with ρ_{ob}^{TOA}, especially in the blue (443 nm). For the green band (560 nm), the simulations were slightly higher than the observations over land surfaces. Most of the lake shows ratios close to unity but decreases toward the shoreline (i.e., simulated < observed). This phenomenon was caused by the threshold that was used to identify the water body of the lake, the pixels' surface reflectance < 0.06 was identified as water leading to the large difference between the measurements of the sampling site and the observations near the shore-land boundary. Because pixels near shores are likely impacted by the mixture of pixels (land), the bottom reflectance, and submerged or floating aquatic vegetation. Bottom reflectance, however, would contribute more in the green band where light penetration is maximum, which is not the case for NIR bands. In contrast, aquatic vegetation would impact red-edge and NIR bands more severely than visible bands. Figure 15 shows the simulation and observation at the sampling station near the middle of the lake. The comparison of the two spectra confirms that the simulation over the sampling station is acceptable. The agreement was particularly good in the NIR and blue bands, but simulated TOA reflectance was slightly lower than the observations in the red and green band. There are some factors that could contribute to the differences between simulations and observations, (1) the surface reflectance of the land, and the aerosol optical thickness at 550 that were retrieved by Sen2Cor could have some errors, and (2) the aerosol optical properties, i.e., the phase function, the angstrom parameter, etc., as well as its vertical profile might not represent perfectly the real ones (3). The assumptions made for the simulations, such as the spatial homogenous atmosphere, and Lambertian surface could also have made some contributions. The combination of the impacts on the simulations is too complicated to be clearly analyzed here. Nonetheless, the differences are acceptable for our purpose of illustrating the magnitude of AE but not modeling.

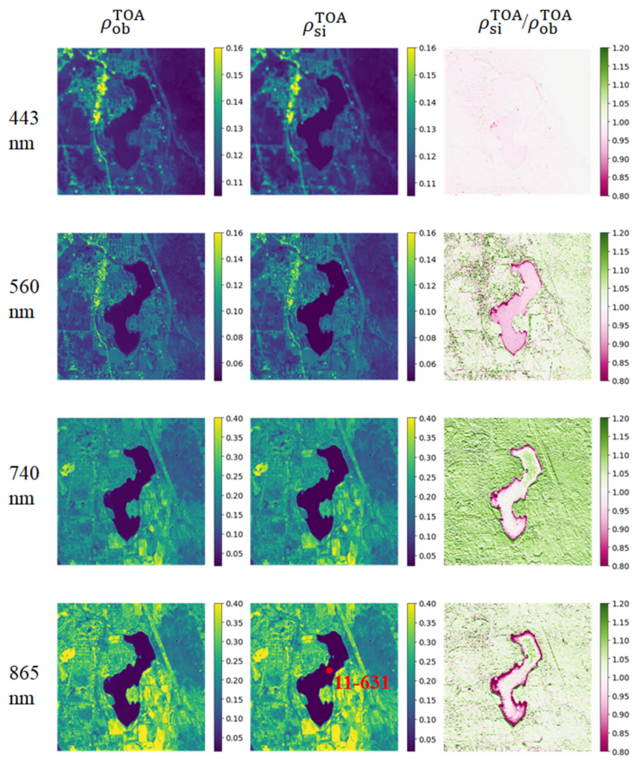

Figure 14. Comparison of the four S2/MSI bands (443 nm, 560 nm, 740 nm, and 865 nm) observed (ρ_{ob}^{TOA}) and the 3-D RTM simulated TOA reflectance (ρ_{si}^{TOA}). The sampling station 11-632 is also shown.

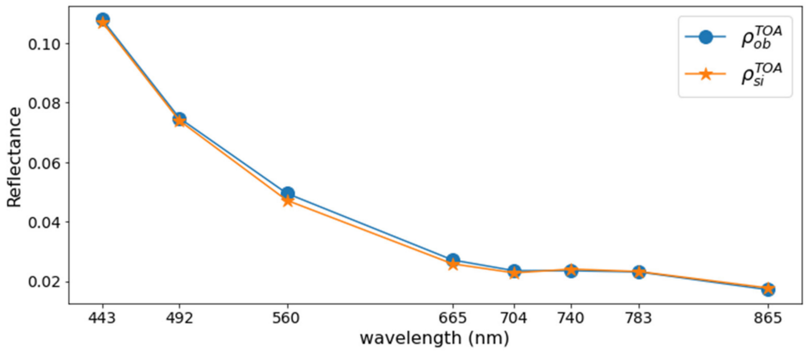

Figure 15. Comparison of the S2/MSI observed (ρ_{ob}^{TOA}) and the simulated TOA reflectance (ρ_{si}^{TOA}) at the location of the sampling station (11-631).

The adjacency reflectance ρ_{adj} is shown in Figure 16. The noisy images found in the shorter wavelength (443 nm and 560 nm) were caused by the same reason explained in Section 3.3.1. As shown, ρ_{adj} has a large difference in different bands, which is the same as the ideal case. However, the ρ_{adj} in 865 nm, are even larger than that of the 5 km^2 lake shown in the ideal case, indicating stronger AE. Compared to the ideal case, the ρ_{adj} has a similar spatial distribution; generally, the near shore is more affected by the adjacency environment which leads to a high value, and the offshore has a lower value. However, the spatial distribution is much more complicated than what the ideal case shows, this is caused by the irregular shape of the lake and the heterogeneous reflectance of the land surfaces. For example, in the NIR band, the narrow southern shore which has a “brighter” land adjacent to the shore shows the largest values of ρ_{adj} and $\xi\rho_t$ which exceed 0.01 and 60%, respectively. The strength of AE varies from band to band, in terms of ρ_{adj} (see Figure 17a), the largest and lowest values are in 783 nm and 665 nm, of which the median values are around 0.004 and 0.01, respectively. Comparing ρ_{adj} to the water reflectance ρ_w (see Figure 17b), the difference is greatest at 865 nm, where the ratio ρ_{adj}/ρ_w exceeds 100, but at 560 nm, the ratio is around 1. Regarding the statistic percent adjacency reflectance $\xi\rho_t$ (see Figure 17c), the difference is greatest at 865 nm, where $\xi\rho_t$ reaches around 60%, while the lowest difference is at 443 nm and the $\xi\rho_t$ is around only 2%.

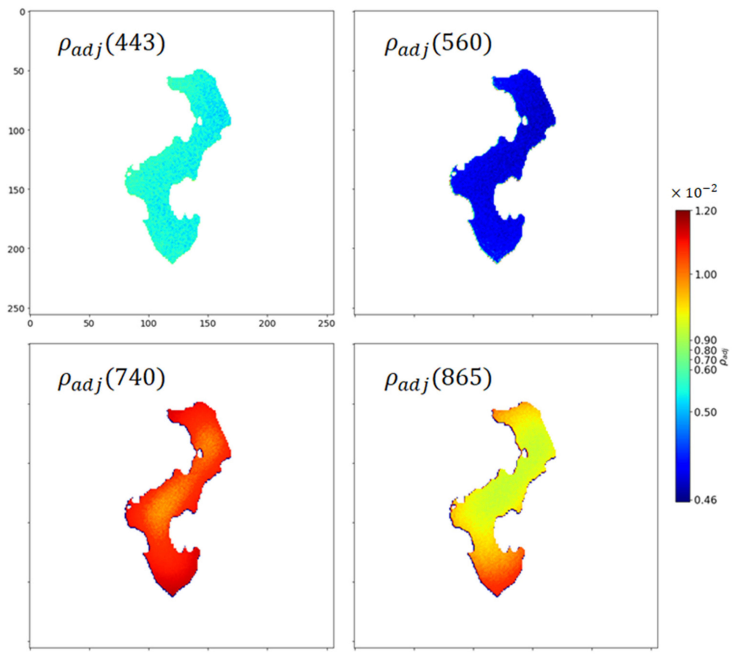

Figure 16. Map of the adjacency reflectance ρ_{adj} of part wavebands (443 nm, 560 nm, 740 nm, and 865 nm) over the lake.

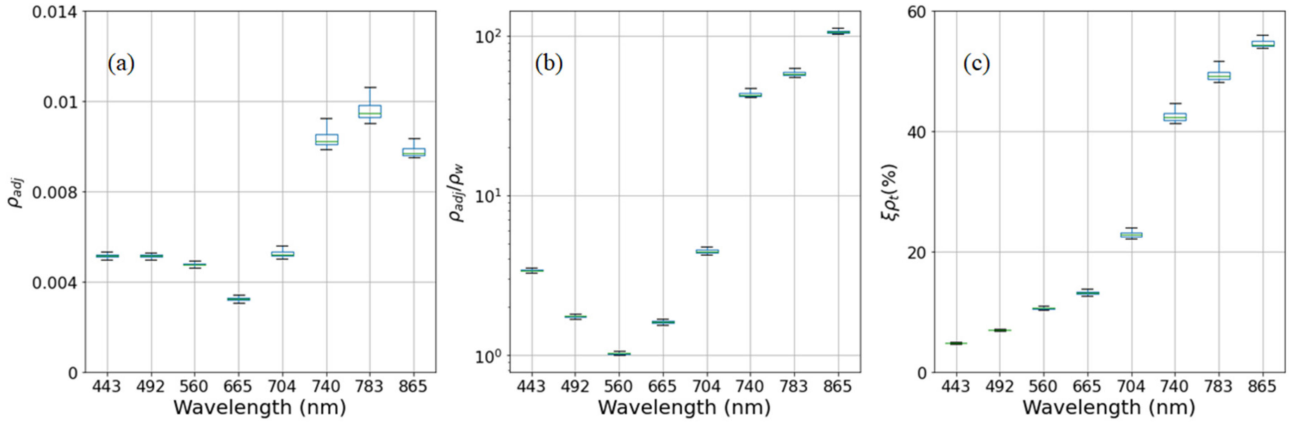

Figure 17. Boxplots of ρ_{adj} (**a**), ρ_{adj}/ρ_w (**b**) and $\xi\rho_t$ (**c**) at different waveband over the lake.

4. Discussion

In this study, the ten available AC algorithms/processors for S2/MSI and L8/OLI were evaluated over small Canadian lakes. The results of the matchup exercise show that the Bias and Errors are very large and often unacceptable while the radiative transfer simulations indicate that the adjacency effects, especially in the NIR bands, over small lakes with clear waters are extremely strong. Here we discuss how the strong AE might affects the AC algorithms, and in this context, the potential improvement of atmospheric correction for small lake application. Some sources that could have caused the uncertainty of the evaluation are discussed as well.

4.1. Sources of Uncertainty

The main source of uncertainty arises from the time window used to match satellite images and sampling. Since too few matchups may reduce the credibility of the statistical results, we used a relatively wide time window of +/− eight days to increase the number of matchups. However, the wide time window will undoubtedly increase the uncertainty of the evaluation, e.g., the extreme weather conditions such as strong winds and heavy rain may cause the resuspension and charge of sediment, which could rapidly change the turbidity of shallow inland waters. This huge uncertainty could have been reduced to some extent by excluding sampling stations with significant precipitation in the time window by visual inspection as described in Section 2.5.2, however, a slight change could be detected in this way. Here, we analyzed the performance of each algorithm for matchups within different intervals to see if the time window has an impact on the performance. No obvious patterns of Errors and SA in terms of intervals were found (see Figure S10 in Supplemental Materials). This suggests that an eight-day time window for L8/OLI and S2/MSI was reasonable for lakes in this study. It is likely that because the errors are so large due to the current limitation of the atmospheric correction algorithms that the variability arising from the changes in the R_{rs}, which must be present, is too small to be observable.

4.2. Adjacency Effects over Small Lakes and Its Influence on Atmospheric Correction

Briefly, AE is caused by the scattering of the atmosphere and the contrast of the surface reflectance between the target and its surrounding environment. Its strength is affected by factors including the aerosol vertical profile and optical thickness, the observation geometry, as well as the contrast of surface reflectance. For a given aerosol type and concentration, the strength of AE is mainly determined by the contrast of surface reflectance. In terms of water bodies including coastal zones and lakes, the distance to the shoreline, and the water and the land surface reflectance all have an impact on the contrast. However, in general, AE over lakes is stronger than that of coastal zones even when they have the same water and land reflectance, this is because the closed shape of the lake allows it to gain more photons from the land (coming from all sides). According to Bulgarelli and Zibordi [90], the maximum $\xi\rho_t$ is approximately 30% in NIR bands based on the simulation for the nearshore coastal waters when the surrounding land is covered with vegetation. The present study shows much larger $\xi\rho_t$ which could reach as much as 60% in NIR for small lakes (see Figure 17). In terms of wavebands, $\rho_{adj}(655)$ are much smaller than $\rho_{adj}(865)$ in the simulations (Section 3.3), this is also mainly because the contrast between the water reflectance and the reflectance of vegetation in the NIR band is much greater at 865 nm than at 655 nm. In fact, a significant difference in the contrast results in the ρ_{adj} not being constant across wavebands but varies from waveband to waveband. As shown in the simulation of the real case, the maximum ρ_{adj} found in the NIR band (783 nm) is around 100 higher than $\rho_w(783)$ and account for 50% of the TOA reflectance. Regarding the minimum ρ_{adj} in the red band, although the absolute value is small, it could not be ignored when compared to the water reflectance ρ_w, 2 to 3 times higher for ρ_{adj} than ρ_w is seen in the simulation (Figure 17b). This implies that ignoring the correction of AE will lead to significant relative errors in the R_{rs} retrieval even for the waveband that may be affected the least by AE.

Although satellite-derived AOTs were not evaluated in this study, the bias was too large compared to the low water-leaving radiance in dark water based on previous inter-comparisons of twelve AC processors validated using the global aerosol robotic network (AERONET) measurements, e.g., the lowest root mean square is 0.119 (ICOR) [90]. There are some reasons that can lead to errors in AC algorithms, such as aerosol models, invalid assumptions, etc. Moreover, AE also has varying degrees of impact on the estimation of aerosols in the existing atmospheric correction algorithms. In terms of the 'NIR black pixel' algorithm implemented in l2gen, theoretical analysis of the propagation of the bias introduced by AE from the NIR bands to the derived path radiance and water-leaving radiance has been given in detail by Bulgarelli et al. [91]. The statistics of the bias based on the AAOT site have shown that bias of the derived path radiance (including aerosol) and water-leaving radiance had a large variability for different situations [51,92]. In general, the path radiance and water-leaving radiance are over- and underestimated, respectively if the land type is not snow or white land. In this study, we examined the STANDARD and the SWIR algorithm in the l2gen processor. Although STANDARD adopts an iterative scheme for processing non-open ocean waters, the first step in the iteration is based on the 'NIR black pixel' assumption, the propagation of the bias will be similar to the previous analysis. However, in the study, because of the stronger AE over small lakes in NIR bands, the aerosol radiance could be severely overestimated, Figure 18 shows the example of sampling site of 11-631 (see Figures 5 and 6). This severe overestimation could result in negative R_{rs} retrieval in VIS bands in the first step of the iteration, especially in the coastal blue and blue bands at which the CDOM absorption is very high Even after setting the concentration of Chla to 10 mg/m^3 and all radiance in the red band (665 nm) assumed to be from the water components (see the source code in l2gen) to re-estimate the water-leaving radiance in NIR-SWIR bands in the second and third iteration, the aerosol was still high and caused negative R_{rs} again (see Figure 18), and the procedure finally terminated. This could explain the failure of STANDARD and SWIR even over clear lake waters (Table 4).

Unlike STANDARD and SWIR, ICOR, SEN2COR, and LaSRC estimate aerosols from land pixels rather than water bodies. Although it may not be affected by AE as much as STANDARD and SWIR because the contrast in brightness between terrestrial pixels may be smaller than that between land and water bodies, it is inevitably affected to some extent, and slight deviations in estimated aerosols can lead to large errors in R_{rs} retrievals for waters. The ACO_DS algorithm estimates the aerosol type and optical thickness from the fitted darkest spectrum (e.g., tree shadows on water) since the darkest spectrum is likely to be to some extent brighter than it actually is due to AE, in addition, the strength of AE is not constant and varies from waveband to waveband, both the aerosol type and optical thickness could be inaccurately estimated. Undoubtedly, quantitative analysis of the bias propagation greatly benefits the understanding of the impacts of AE on AC algorithms. However, the strategy and complexity of a specific AC algorithm sometimes determine the difficulty of the quantitative analysis, for example, unlike STANDARD and SWIR, the other algorithms in this study either retrieve aerosol based on the pixels of the entire subscene but not on single pixels (e.g., ACOLITE, Sen2cor, ICOR), or retrieve Rrs on the coupled atmosphere-water system using specific optimization (POLYMER) or regression technique (NN). This determines that the propagation of biases is almost impossible to derive and express in algebraic form like the 'black pixel' algorithm. Some experiments could be potentially performed to study the statistic bias introduced by AE, for example, the simulated TOA image based on the 3D radiative transfer model could be used to quantify the impact of AE on ACOLITE. However, the main difficulty is that the processors can only accept the official release of the level-1 image as input, which means studying the impact of AE by comparing the outputs (AOT and R_{rs}) from the TOA reflectance with and without AE requires a lot of extra works to adapt the source code.

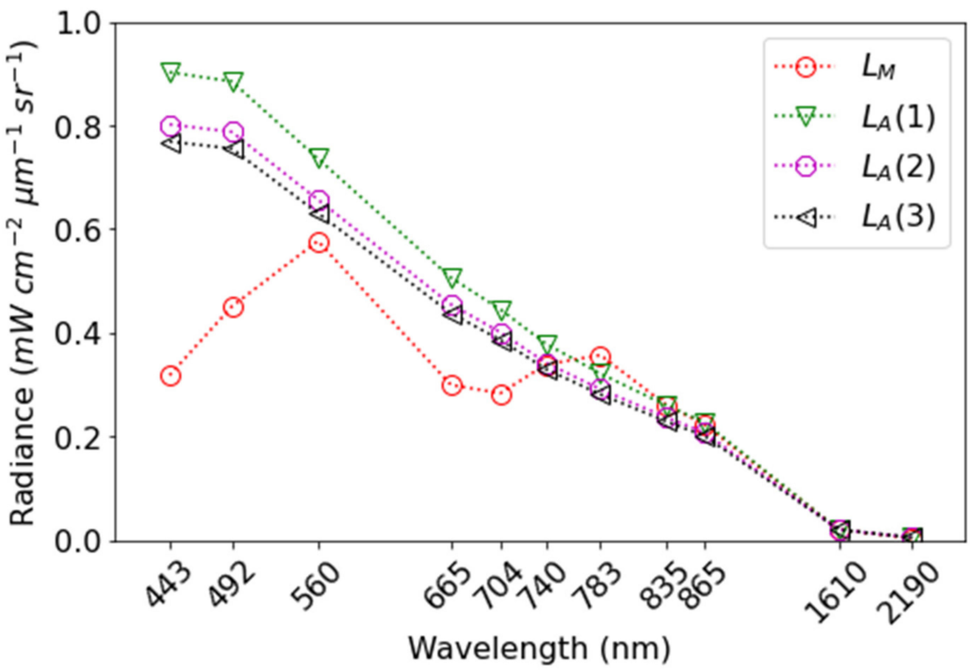

Figure 18. STANDARD-derived radiance of aerosol L_A for the first (green), second (purple), and third iteration (black) in the iterative scheme for the sampling station of 11-631. The TOA radiance after correction of Rayleigh scattering, and gas absorption (L_M) is also shown (red).

For the algorithms that directly retrieve R_{rs} not relying on the estimation of aerosol, they are affected by AE as well. As shown in Figs. 10 and 12, C2RCC and C2X, or POLYMER have minimum errors in the derived R_{rs} in NIR bands and seem less affected by AE, this could be explained by the predefined water model in the algorithms and thus the magnitude of the derived R_{rs} in NIR bands are always in the range of the predefined water model. However, since the reflectance contaminated by the non-constant strength of AE spectrum is taken into account to directly derive R_{rs} by the neural network model or nonlinear optimization, the algorithms will nevertheless be affected by AE although it is unclear how it is affected, i.e., a totally incorrect R_{rs} spectrum shape may be derived while the magnitude in NIR bands is correct.

4.3. Potential Method of Improvement

As analyzed above, AE can have a non-negligible impact on atmospheric correction. The work compared matchup results with and without correcting for simulated AE, showing consistent improvements in the retrieval of R_{rs} [89] However, unfortunately, only a few operational correction algorithms are currently available. For the algorithms that were selected for the evaluation exercise, only SEN2COR and ICOR_SM include the AE correction procedure. SEN2COR integrates the RICHTER1990-based algorithm for AE correction, this method approximates the adjacency reflectance ρ_{adj} as the difference between the reflectance of the target (pixel) and the reflectance of its surroundings.

$$\rho_{adj} = q\left(\rho_{pc} - \overline{\rho}_{pc}\right) \tag{16}$$

where, q refers to the ratio of the diffuse to direct transmittance towards the sensor, ρ_{pc} refers to the surface reflectance of the target retrieved from the TOA reflectance without considering AE, and $\overline{\rho}_{pc}$ refers to the weighted average of ρ_{pc} surrounding the target in a range of N pixels, which is needed to be specified before running the correction. This method is well described in the ATCOR Theoretical Background Document [82]. ICOR_SM integrates the SIMEC algorithm, which was first proposed by Sterckx et al. [49] for the correction of high-resolution airborne imaging spectroscopy data. It estimates the contribution of the background radiance in a range of N pixels. However, unlike SEN2COR, the range of N is not fixed but determined by an iterative method based on the correspondence with the NIR similarity spectrum. The advantage of SIMEC is that it does not have to make assumptions about NIR albedo, so it can be applied in moderately turbid waters, but a constant NIR reflectance ratio may not be valid for some situations, e.g., waters with macrophyte growth or specific algae blooms and areas where bottom reflection is significant in the NIR.

Both RICHTER1990 and SIMEC provide rational methods for the estimation of ρ_{adj}, but the correction processing requires knowledge of aerosol (type and optical thickness), which is one of the main factors that determines the strength of AE. However, an aerosol is always unknown and needs to be retrieved from the imagery itself by the AC algorithm. In Sen2Cor and ICOR_SM, the aerosol is determined by the land-based aerosol retrieval method, although the land pixel may be affected less by AE, the effect is inevitable when the surface is heterogeneous, and therefore the aerosol could be inaccurately derived. Using inaccurate aerosol to estimate ρ_{adj} will undoubtedly introduce uncertainty into it. This may explain that the ICOR_SM does not give a satisfying result in this study, though it is better than ICOR. It is worth mentioning that the SEN2COR generates the same results for R_{rs} with the AE correction function ON or OFF, and it is not clear if it is caused by bugs in the SNAP implementation. One of the potential solutions to improve the atmospheric correction for small lakes is to retrieve aerosol considering AE, in other words, to couple the procedures of traditional atmospheric correction and AE correction instead of treating them separately. Global optimization techniques or iterative schemes could be employed to solve the unknowns in the coupled procedure.

5. Conclusions

A large amount of good quality R_{rs} spectra (>300) has been collected in Canadian lakes from three LakePulse fieldwork campaigns (2017–2019). In this study, the dataset was used to evaluate AC algorithms for L8/OLI and S2/MSI imagery. The primary version of this data set (2017 and 2018) was considered in the ACIX-Aqua intercomparison presented by Pahlevan et al. [34], but all the matchups were excluded from the final analysis due to the large error in the water retrievals. The current paper included the data from 2019 and was reprocessed and quality controlled, here we further explore the reasons why AC failed over lakes sampled in LakePulse. By relaxing the matchups criterion in terms of the time difference between in situ and satellite acquisition, we were able to obtain enough data points to perform a statistical analysis of the performance of ten AC algorithm configurations for both Landsat-8 (N = 214) and Sentinel-2 (N = 413) images.

The results from the evaluation exercise showed that all algorithms failed to meet the requirements of retrieval accuracy when a threshold of 30% uncertainty is taken (https://gcos.wmo.int/en/essential-climate-variables/about/requirements, accessed on 10 May 2022), actually, even the minimum error (>100%) is significantly larger than that. However, some interesting findings must be emphasized. Generally, as far as the visible bands are concerned, ACO_DS is better at preserving spectrum shape than other AC algorithms, while C2RCC and C2X are better in terms of magnitude. Radiative transfer simulations showed that AE over small lakes is much more significant than in coastal regions. The significant AE is likely the main reason that leads to the failure of all AC algorithms, although other issues such as the aerosol model, calibration of the sensor, and instrument stray light contamination could also contribute to it. AE correction must be taken into account to improve the existing algorithms for small lakes. Unfortunately, most processors do not include AE correction, and available AE correction algorithms are rare. As far as we know, ICOR_SM and the algorithm implemented in Sen2Cor are the only operational ones. However, they both have a limitation in common (i.e., treating the aerosol retrieval and AE estimation separately). This will be improved by integrating the AE estimation into the aerosol retrieval, which may be one of the directions where more efforts should be directed for the next generation of atmospheric corrections for inland waters.

Supplementary Materials: The following supporting information can be downloaded at: https://www.mdpi.com/article/10.3390/rs14132979/s1, Figure S1: Extinction coefficient profile due to rayleigh scattering (left) and the total gas absorption coefficient profile (right); Figure S2: The extinction coefficient profile due to aerosol scattering with AOT = 0.06; Figure S3: Surface reflectance in the L8/OLI VNIR bands for the simulation; Figure S4: Surface reflectance in the S2/MSI VNIR bands for the simulation; Figure S5: Scatter plots of the in situ measured R_{rs} and the R_{rs} retrieved by different algorithms in Landsat-8 OLI bands for the G-ALL group; Figure S6: Scatter plots of the in situ measured R_{rs} and the R_{rs} retrieved by different algorithms in Landsat-8 OLI bands for the G-CIRRUS group; Figure S7: Scatter plots of the in situ measured R_{rs} and the R_{rs} retrieved by different algorithms in Sentinel-2 MSI bands for the G-ALL group; Figure S8: Scatter plots of the in situ measured R_{rs} and the R_{rs} retrieved by different algorithms in Sentinel-2 MSI bands for the G-CIRRUS group; Figure S9: Error and SA for matchups with different intervals.

Author Contributions: Conceptualization, Y.P., S.B. and Y.H.; methodology, Y.P. and S.B.; software, Y.P.; validation, Y.P., S.B. and Y.H.; formal analysis, Y.P.; investigation, Y.P.; resources, Y.P.; data curation, Y.P.; writing—original draft preparation, Y.P.; writing—review and editing, Y.P., S.B. and Y.H.; visualization, Y.P.; supervision, S.B.; project administration, Y.H. and S.B.; funding acquisition, Y.H., and S.B. All authors have read and agreed to the published version of the manuscript.

Funding: This research was funded by the Natural Sciences and Engineering Research Council of Canada (NSERC) Canadian Lake Pulse Network grant number NETGP 479720-15, NSERC discovery grant to S.B. RGPIN-2019-06070, and also funded by Canadian Space Agency (CSA)—Flights and Fieldwork for the Advancement of Science and Technology program (FAST) grant number FARIMA18.

Data Availability Statement: Validation data from Lake Pulse are available from the corresponding author only after permissions have been granted from the Lake Pulse Network.

Acknowledgments: This work was financially supported by NSERC through the Canadian Lake Pulse Network Strategic Partnership Network program. Many thanks to the LakePulse field team participants for their hard work in obtaining in-situ measurements. We thank Geneviève Potvin and Bruno Cremella for providing the CDOM and Chla, and Maxime Fradette for preparing the maps. Thanks to three anonymous reviewers for their comments and suggestions on a previous version of this manuscript. This work was also supported by NSERC discovery grant to SB (RGPIN-2019-06070) and Canadian Space Agency (CSA)—Flights and Fieldwork for the Advancement of Science and Technology program (FAST, FARIMA18).

Conflicts of Interest: The authors declare no conflict of interest.

References

1. Dörnhöfer, K.; Oppelt, N. Remote sensing for lake research and monitoring—Recent advances. *Ecol. Indic.* **2016**, *64*, 105–122. [CrossRef]
2. Wrilegy, R.C.; Horne, A.J. Remote sensing and lake eutrophication. *Nature* **1974**, *250*, 213–214. [CrossRef]
3. Brönmark, C.; Hansson, L.A. Environmental issues in lakes and ponds: Current state and perspectives. *Environ. Conserv.* **2002**, *29*, 290–307. [CrossRef]

4. Dudgeon, D.; Arthington, A.H.; Gessner, M.O.; Kawabata, Z.I.; Knowler, D.J.; Lévêque, C.; Naiman, R.J.; Prieur-Richard, A.H.; Soto, D.; Stiassny, M.L.J.; et al. Freshwater biodiversity: Importance, threats, status and conservation challenges. *Biol. Rev. Camb. Philos. Soc.* **2006**, *81*, 163–182. [CrossRef]
5. U.S. Senate. *Federal Water Pollution Control Act, 33 U.S.C. 1251 et seq*; U.S. Senate: Washington, DC, USA, 2002.
6. Government of South Africa. *National Water Act*; Government of South Africa: Pretoria, South Africa, 1998.
7. Australian Government. *National Water Management Strategy of Australia and New Zealand*; Australian Government: Canberra, Australia, 2000.
8. European Commission. *Directive 2000/60/EC of the European Parliament and of the Council of 23 October 2000 Establishing a Framework for Community Action in the Field of Water Policy 2000*; European Commission: Brussels, Belgium, 2000.
9. Huot, Y.; Brown, C.A.; Potvin, G.; Antoniades, D.; Baulch, H.M.; Beisner, B.E.; Bélanger, S.; Brazeau, S.; Cabana, H.; Cardille, J.A.; et al. The NSERC Canadian Lake Pulse Network: A national assessment of lake health providing science for water management in a changing climate. *Sci. Total Environ.* **2019**, *695*, 133668. [CrossRef]
10. Topp, S.N.; Pavelsky, T.M.; Jensen, D.; Simard, M.; Ross, M.R.V. Research trends in the use of remote sensing for inland water quality science: Moving towards multidisciplinary applications. *Water* **2020**, *12*, 169. [CrossRef]
11. Scarpace, F.L.; Holmquist, K.W.; Fisher, L.T. Landsat analysis of lake quality. *Photogramm. Eng. Remote Sens.* **1979**, *45*, 623–633.
12. Binding, C.E.; Greenberg, T.A.; Watson, S.B.; Rastin, S.; Gould, J. Long term water clarity changes in North America's Great Lakes from multi-sensor satellite observations. *Limnol. Oceanogr.* **2015**, *60*, 1976–1995. [CrossRef]
13. Jones, M.O. Application of MODIS for Monitoring Water Quality of a Large Oligotrophic Lake. Graduate Student Thesis, University of Montana, Missoula, MT, USA, 2006.
14. Cardille, J.A.; Leguet, J.; Giorgio, P.; Cardille, J.A.; Leguet, J.; Remote, G.; Cardille, J.A.; Leguet, J.; Giorgio, P. Remote sensing of lake CDOM using noncontemporaneous field data. *Can. J. Remote Sens.* **2013**, *39*, 118–126. [CrossRef]
15. Brivio, P.A.; Giardino, C.; Zilioli, E. Determination of chlorophyll concentration changes in Lake Garda using an image-based radiative transfer code for Landsat TM images. *Int. J. Remote Sens.* **2001**, *22*, 487–502. [CrossRef]
16. Ungar, S.G.; Pearlman, J.S.; Mendenhall, J.A.; Reuter, D. Overview of the Earth Observing One (EO-1) mission. *IEEE Trans. Geosci. Remote Sens.* **2003**, *41*, 1149–1159. [CrossRef]
17. Zhao, D.; Cai, Y.; Jiang, H.; Xu, D.; Zhang, W.; An, S. Estimation of water clarity in Taihu Lake and surrounding rivers using Landsat imagery. *Adv. Water Resour.* **2011**, *34*, 165–173. [CrossRef]
18. Deutsch, E.S.; Cardille, J.A.; Koll-Egyed, T.; Fortin, M.J. Landsat 8 lake water clarity empirical algorithms: Large-scale calibration and validation using government and citizen science data from across Canada. *Remote Sens.* **2021**, *13*, 1257. [CrossRef]
19. Koll-Egyed, T.; Cardille, J.A.; Deutsch, E. Multiple images improve lake CDOM estimation: Building better landsat 8 empirical algorithms across southern canada. *Remote Sens.* **2021**, *13*, 3615. [CrossRef]
20. Bresciani, M.; Adamo, M.; De Carolis, G.; Matta, E.; Pasquariello, G.; Vaičiute, D.; Giardino, C. Monitoring blooms and surface accumulation of cyanobacteria in the Curonian Lagoon by combining MERIS and ASAR data. *Remote Sens. Environ.* **2014**, *146*, 124–135. [CrossRef]
21. Chen, J.; Quan, W. Using Landsat/TM imagery to estimate nitrogen and phosphorus concentration in Taihu Lake, China. *IEEE J. Sel. Top. Appl. Earth Obs. Remote Sens.* **2012**, *5*, 273–280. [CrossRef]
22. Kloiber, S.M.; Brezonik, P.L.; Bauer, M.E. Application of Landsat imagery to regional-scale assessments of lake clarity. *Water Res.* **2002**, *36*, 4330–4340. [CrossRef]
23. Kloiber, S.M.; Brezonik, P.L.; Olmanson, L.G.; Bauer, M.E. A procedure for regional lake water clarity assessment using Landsat multispectral data. *Remote Sens. Environ.* **2002**, *82*, 38–47. [CrossRef]
24. Lathrop, R.G. Landsat Thematic Mapper monitoring of turbid inland water quality. *Photogramm. Eng. Remote Sens.* **1992**, *58*, 465–470.
25. Lillesand, T.M.; Johnson, W.L.; Deuell, R.L. Use of landsat data to predict the trophic state of Minnesota lakes. *Photogramm. Eng. Remote Sens.* **1983**, *49*, 219–229.
26. Ma, R.; Duan, H.; Gu, X.; Zhang, S. Detecting aquatic vegetation changes in Taihu lake, China using multi-temporal satellite imagery. *Sensors* **2008**, *8*, 3988–4005. [CrossRef] [PubMed]
27. Menken, K.D.; Brezonik, P.L.; Bauer, M.E. Influence of chlorophyll and colored dissolved organic matter (CDOM) on lake reflectance spectra: Implications for measuring lake properties by remote sensing. *Lake Reserv. Manag.* **2006**, *22*, 179–190. [CrossRef]
28. Franz, B.A.; Bailey, S.W.; Kuring, N.; Werdell, P.J. Ocean Color Measurements from Landsat-8 OLI using SeaDAS. *Proc. Ocean Opt.* **2014**, *12*, 26–31.
29. Antoine, D.; Morel, A. A multiple scattering algorithm for atmospheric correction of remotely sensed ocean colour (MERIS instrument): Principle and implementation for atmospheres carrying various aerosols including absorbing ones. *Int. J. Remote Sens.* **1999**, *20*, 1875–1916. [CrossRef]
30. Gordon, H.R.; Castaho, D.J. Coastal Zone Color Scanner atmospheric correction algorithm: Multiple scattering effects. *Appl. Opt.* **1987**, *26*, 2111–2122. [CrossRef]
31. Mobley, C.D.; Werdell, J.; Franz, B.; Ahmad, Z.; Bailey, S. *Atmospheric Correction for Satellite Ocean Color Radiometry*; A Tutorial and Documentation of the Algorithms Used by the NASA Ocean Biology Processing Group; National Aeronautics and Space Administration: Greenbelt, MD, USA, 2016; pp. 1–73.

32. McClain, C.R.; Hooker, S.; Feldman, G.; Bontempi, P. Satellite data for ocean biology, biogeochemistry, and climate research. *Eos* **2006**, *87*, 340–342. [CrossRef]
33. Mouw, C.B.; Greb, S.; Aurin, D.; Digiacomo, P.M.; Lee, Z.; Twardowski, M.; Binding, C.; Hu, C.; Ma, R.; Moore, T.; et al. Remote Sensing of Environment Aquatic color radiometry remote sensing of coastal and inland waters: Challenges and recommendations for future satellite missions. *Remote Sens. Environ.* **2015**, *160*, 15–30. [CrossRef]
34. Pahlevan, N.; Mangin, A.; Balasubramanian, S.V.; Smith, B.; Alikas, K.; Arai, K.; Barbosa, C.; Bélanger, S.; Binding, C.; Bresciani, M.; et al. ACIX-Aqua: A global assessment of atmospheric correction methods for Landsat-8 and Sentinel-2 over lakes, rivers, and coastal waters. *Remote Sens. Environ.* **2021**, *258*, 112366. [CrossRef]
35. Warren, M.A.; Simis, S.G.H.; Martinez-Vicente, V.; Poser, K.; Bresciani, M.; Alikas, K.; Spyrakos, E.; Giardino, C.; Ansper, A. Assessment of atmospheric correction algorithms for the Sentinel-2A MultiSpectral Imager over coastal and inland waters. *Remote Sens. Environ.* **2019**, *225*, 267–289. [CrossRef]
36. Pereira-Sandoval, M.; Ruescas, A.; Urrego, P.; Ruiz-Verdú, A.; Delegido, J.; Tenjo, C.; Soria-Perpinyà, X.; Vicente, E.; Soria, J.; Moreno, J. Evaluation of atmospheric correction algorithms over spanish inland waters for sentinel-2 multi spectral imagery data. *Remote Sens.* **2019**, *11*, 1469. [CrossRef]
37. Doerffer, R.; Schiller, H. The MERIS case 2 water algorithm. *Int. J. Remote Sens.* **2007**, *28*, 517–535. [CrossRef]
38. Brockmann, C.; Doerffer, R.; Peters, M.; Stelzer, K.; Embacher, S.; Ruescas, A. Evolution of the C2RSS Neural Network for Sentinel 2 and 3 for the Ritreval of Ocean Color Products in Normal and Extreme Optically Complex Waters. In Proceedings of the Living Planet Symposium 2016, Prague, Czech Republic, 9–13 May 2016.
39. Steinmetz, F.; Deschamps, P.-Y.; Ramon, D. (POLYMER)Atmospheric correction in presence of sun glint: Application to MERIS. *Opt. Express* **2011**, *19*, 9783–9800. [CrossRef] [PubMed]
40. Vanhellemont, Q.; Ruddick, K. Atmospheric correction of metre-scale optical satellite data for inland and coastal water applications. *Remote Sens. Environ.* **2018**, *216*, 586–597. [CrossRef]
41. De Keukelaere, L.; Sterckx, S.; Adriaensen, S.; Knaeps, E.; Reusen, I.; Giardino, C.; Bresciani, M.; Hunter, P.; Neil, C.; Van Der Zande, D.; et al. Atmospheric correction of Landsat-8/OLI and Sentinel-2/MSI data using iCOR algorithm: Validation for coastal and inland waters. *Eur. J. Remote Sens.* **2018**, *51*, 525–542. [CrossRef]
42. Main-Knorn, M.; Pflug, B.; Louis, J.; Debaecker, V.; Müller-Wilm, U.; Gascon, F. Sen2Cor for Sentinel-2. In *Image and Signal Processing for Remote Sensing*; SPIE: Bellingham, WA, USA, 2017; p. 3.
43. Otterman, J.; Fraser, R.S. Adjacency effects on imaging by surface reflection and atmospheric scattering: Cross radiance to zenith. *Appl. Opt.* **1979**, *18*, 2852. [CrossRef] [PubMed]
44. Santer, R.; Schmechtig, C. Adjacency effects on water surfaces: Primary scattering approximation and sensitivity study. *Appl. Opt.* **2000**, *39*, 361. [CrossRef] [PubMed]
45. Tanré, D.; Herman, M.; Deschamps, P.Y. Influence of the background contribution upon space measurements of ground reflectance. *Appl. Opt.* **1981**, *20*, 3676. [CrossRef]
46. Tanré, D.; Deschamps, P.Y.; Duhaut, P.; Herman, M. Adjacency effect produced by the atmospheric scattering in thematic mapper data. *J. Geophys. Res.* **1987**, *92*, 12000–12006. [CrossRef]
47. Kiselev, V.; Bulgarelli, B.; Heege, T. Sensor independent adjacency correction algorithm for coastal and inland water systems. *Remote Sens. Environ.* **2015**, *157*, 85–95. [CrossRef]
48. Reinersman, P.N.; Carder, K.L. Monte Carlo simulation of the atmospheric point-spread function with an application to correction for the adjacency effect. *Appl. Opt.* **1995**, *34*, 4453. [CrossRef]
49. Sterckx, S.; Knaeps, S.; Kratzer, S.; Ruddick, K. SIMilarity Environment Correction (SIMEC) applied to MERIS data over inland and coastal waters. *Remote Sens. Environ.* **2015**, *157*, 96–110. [CrossRef]
50. Bulgarelli, B.; Kiselev, V.; Zibordi, G. Simulation and analysis of adjacency effects in coastal waters: A case study. *Appl. Opt.* **2014**, *53*, 1523–1545. [CrossRef] [PubMed]
51. Bulgarelli, B.; Zibordi, G. On the detectability of adjacency effects in ocean color remote sensing of mid-latitude coastal environments by SeaWiFS, MODIS-A, MERIS, OLCI, OLI and MSI. *Remote Sens. Environ.* **2018**, *209*, 423–438. [CrossRef]
52. Bulgarelli, B. Seasonal Impact of Adjacency Effects on Ocean Color Radiometry at the AAOT Validation Site. *IEEE Geosci. Remote Sens. Lett.* **2018**, *15*, 488–492. [CrossRef]
53. Richter, R. A fast atmospheric correction algorithm applied to landsat tm images. *Int. J. Remote Sens.* **1990**, *11*, 159–166. [CrossRef]
54. Minomura, M.; Kuze, H.; Takeuchi, N. Adjacency effect in the atmospheric correction of satellite remote sensing data: Evaluation of the influence of aerosol extinction profiles. *Opt. Rev.* **2001**, *8*, 133–141. [CrossRef]
55. Mousivand, A.; Verhoef, W.; Menenti, M.; Gorte, B. Modeling Top of Atmosphere Radiance over Heterogeneous Non-Lambertian Rugged Terrain. *Remote Sens.* **2015**, *7*, 8019–8044. [CrossRef]
56. Bulgarelli, B.; Zibordi, G. Adjacency radiance around a small island: Implications for system vicarious calibrations. *Appl. Opt.* **2020**, *59*, C63. [CrossRef]
57. Kuhn, C.; Matos, A.; De Ward, N.; Loken, L.; Oliveira, H.; Kampel, M.; Richey, J.; Stadler, P.; Crawford, J.; Striegl, R.; et al. Performance of Landsat-8 and Sentinel-2 surface reflectance products for river remote sensing retrievals of chlorophylla and turbidity. *Remote Sens. Environ.* **2019**, *224*, 104–118. [CrossRef]

58. Sun, B.; Schäfer, M.; Ehrlich, A.; Jäkel, E.; Wendisch, M. Influence of atmospheric adjacency effect on top-of-atmosphere radiances and its correction in the retrieval of Lambertian surface reflectivity based on three-dimensional radiative transfer. *Remote Sens. Environ.* **2021**, *263*, 112543. [CrossRef]
59. Statistics Canada. *Ecological Land Classification, 2017*; Statistics Canada: Ottava, ON, Canada, 2018; ISBN 9780660245010.
60. McColl, R.W. *Encyclopedia of World Geography*; Infobase Publishing: New York, NY, USA, 2015; ISBN 978-0-8160-5786-3.
61. Morrow, J.H.; Booth, C.R.; Lind, R.N.; Hooker, S.B.; Profiling, O.; In, S.C.; Hooker, S.B.; Booth, C.R. The Compact-Optical Profiling System (C-OPS). In *Advances in Measuring the Apparent Optical Properties (AOPs) of Optically Complex Waters, NASA Tech.Memo*; Biospherical Instruments Inc: 2010–215856; NASA Goddard Space Flight Center: Greenbelt, MD, USA, 2010; pp. 42–50.
62. Ruddick, K.G.; Voss, K.; Banks, A.C.; Boss, E.; Castagna, A.; Frouin, R.; Hieronymi, M.; Jamet, C.; Johnson, B.C.; Kuusk, J.; et al. A Review of Protocols for Fiducial Reference Measurements of Downwelling Irradiance for the Validation of Satellite Remote Sensing Data over Water. *Remote Sens.* **2019**, *11*, 1742. [CrossRef]
63. Spyrakos, E.; O'Donnell, R.; Hunter, P.D.; Miller, C.; Scott, M.; Simis, S.G.H.; Neil, C.; Barbosa, C.C.F.; Binding, C.E.; Bradt, S.; et al. Optical types of inland and coastal waters. *Limnol. Oceanogr.* **2018**, *63*, 846–870. [CrossRef]
64. Franz, B.A.; Bailey, S.W.; Kuring, N.; Werdell, P.J. Ocean color measurements with the Operational Land Imager on Landsat-8: Implementation and evaluation in SeaDAS. *J. Appl. Remote Sens.* **2015**, *9*, 096070. [CrossRef]
65. Pahlevan, N.; Sarkar, S.; Franz, B.A.; Balasubramanian, S.V.; He, J. Sentinel-2 MultiSpectral Instrument (MSI) data processing for aquatic science applications: Demonstrations and validations. *Remote Sens. Environ.* **2017**, *201*, 47–56. [CrossRef]
66. Hooker, S.B.; Morrow, J.H.; Matsuoka, A. Apparent optical properties of the Canadian Beaufort Sea—Part 2: The 1% and 1 cm perspective in deriving and validating AOP data products. *Biogeosciences* **2013**, *10*, 4511–4527. [CrossRef]
67. Morel, A.; Gentili, B. Diffuse reflectance of oceanic waters II Bidirectional aspects. *Appl. Opt.* **1993**, *32*, 6864. [CrossRef] [PubMed]
68. Mueller, J.L.; Austin, R.W.; Morel, A.Y.; Fargion, G.S.; McClain, C.R. *Ocean Optics Protocols for Satellite Ocean Color Sensor Validation, Revision 4, Volume I: Introduction, Background and Conventions*; Nasa/Tm-2003-21621; NASA Goddard Space Flight Center: Greenbelt, MD, USA, 2003; Volume I, p. 56.
69. Morel, A.; Maritorena, S. Bio-optical properties of oceanic waters: A reappraisal. *J. Geophys. Res. Ocean.* **2001**, *106*, 7163–7180. [CrossRef]
70. Mobley, C.D. Estimation of the remote-sensing reflectance from above-surface measurements. *Appl. Opt.* **1999**, *38*, 7442–7455. [CrossRef]
71. Ruddick, K.G.; De Cauwer, V.; Park, Y.J.; Moore, G. Seaborne measurements of near infrared water-leaving reflectance: The similarity spectrum for turbid waters. *Limnol. Oceanogr.* **2006**, *51*, 1167–1179. [CrossRef]
72. Simis, S.G.H.; Olsson, J. Unattended processing of shipborne hyperspectral reflectance measurements. *Remote Sens. Environ.* **2013**, *135*, 202–212. [CrossRef]
73. Kutser, T.; Vahtmäe, E.; Paavel, B.; Kauer, T. Removing glint effects from field radiometry data measured in optically complex coastal and inland waters. *Remote Sens. Environ.* **2013**, *133*, 85–89. [CrossRef]
74. Jiang, D.; Matsushita, B.; Yang, W. A simple and effective method for removing residual reflected skylight in above-water remote sensing reflectance measurements. *ISPRS J. Photogramm. Remote Sens.* **2020**, *165*, 16–27. [CrossRef]
75. Lee, Z.; Carder, K.L.; Arnone, R.A. (QAA)Deriving Inherent Optical Properties from Water Color: A Multiband Quasi-Analytical Algorithm for Optically Deep Waters. *Appl. Opt.* **2002**, *41*, 5755. [CrossRef] [PubMed]
76. Bailey, S.W.; Franz, B.A.; Werdell, P.J. Estimation of near-infrared water-leaving reflectance for satellite ocean color data processing. *Opt. Express* **2010**, *18*, 7521–7527. [CrossRef] [PubMed]
77. Siegel, D.A.; Wang, M.; Maritorena, S.; Robinson, W. Atmospheric correction of satellite ocean color imagery: The black pixel assumption. *Appl. Opt.* **2000**, *39*, 3582–3591. [CrossRef] [PubMed]
78. Wang, M.; Shi, W.; Son, S. Evaluation of MODIS SWIR and NIR-SWIR atmospheric correction algorithms using SeaBASS data. *Remote Sens. Environ.* **2009**, *113*, 635–644. [CrossRef]
79. Vanhellemont, Q. Adaptation of the dark spectrum fitting atmospheric correction for aquatic applications of the Landsat and Sentinel-2 archives. *Remote Sens. Environ.* **2019**, *225*, 175–192. [CrossRef]
80. U.S. Geological Survey. *Landsat 8 Surface Reflectance Code (LASRC) Poduct Guide*; No. LSDS-1368 Version 2.0; U.S. Geological Survey: Reston, VA, USA, 2019; p. 40.
81. Mayer, B.; Kylling, A. Technical note: The libRadtran software package for radiative transfer calculations—Description and examples of use. *Atmos. Chem. Phys.* **2006**, *5*, 1855–1877. [CrossRef]
82. Richter, R.; Schlapfer, D. Atmospheric and topographic correction (ATCOR theoretical background document). *DLR IB* **2020**, *1*, 0564-03.
83. Sterckx, S.; Knaeps, E.; Adriaensen, S.; Reusen, I.; De Keukelaere, L.; Hunter, P.; Giardino, C.; Odermatt, D. Opera: An atmospheric correction for land and water. *Proc. Sentin. Sci. Work.* **2015**, *1*, 3–6.
84. Guanter, L. *New Algorithms for Atmospheric Correction and Retrieval of Biophysical Parameters in Earth Observation. Application to ENVISAT/MERIS Data*; Universitat de Valencia: Valencia, Spain, 2006.
85. Olmanson, L.G.; Bauer, M.E.; Brezonik, P.L. A 20-year Landsat water clarity census of Minnesota's 10,000 lakes. *Remote Sens. Environ.* **2008**, *112*, 4086–4097. [CrossRef]
86. Sriwongsitanon, N.; Surakit, K.; Thianpopirug, S. Influence of atmospheric correction and number of sampling points on the accuracy of water clarity assessment using remote sensing application. *J. Hydrol.* **2011**, *401*, 203–220. [CrossRef]

87. Tebbs, E.J.; Remedios, J.J.; Harper, D.M. Remote sensing of chlorophyll-a as a measure of cyanobacterial biomass in Lake Bogoria, a hypertrophic, saline-alkaline, flamingo lake, using Landsat ETM+. *Remote Sens. Environ.* **2013**, *135*, 92–106. [CrossRef]
88. Ahmad, Z.; Franz, B.A.; McClain, C.R.; Kwiatkowska, E.J.; Werdell, J.; Shettle, E.P.; Holben, B.N. New aerosol models for the retrieval of aerosol optical thickness and normalized water-leaving radiances from the SeaWiFS and MODIS sensors over coastal regions and open oceans. *Appl. Opt.* **2010**, *49*, 5545–5560. [CrossRef]
89. Kavzoglu, T. Simulating Landsat ETM+ imagery using DAIS 7915 hyperspectral scanner data. *Int. J. Remote Sens.* **2004**, *25*, 5049–5067. [CrossRef]
90. Doxani, G.; Vermote, E.; Roger, J.C.; Gascon, F.; Adriaensen, S.; Frantz, D.; Hagolle, O.; Hollstein, A.; Kirches, G.; Li, F.; et al. Atmospheric correction inter-comparison exercise. *Remote Sens.* **2018**, *10*, 352. [CrossRef]
91. Bulgarelli, B.; Zibordi, G.; Mélin, F. On the minimization of adjacency effects in SeaWiFS primary data products from coastal areas. *Opt. Express* **2018**, *26*, 301–313. [CrossRef]
92. Bulgarelli, B.; Kiselev, V.; Zibordi, G. Adjacency effects in satellite radiometric products from coastal waters: A theoretical analysis for the northern Adriatic Sea. *Appl. Opt.* **2017**, *56*, 854. [CrossRef]